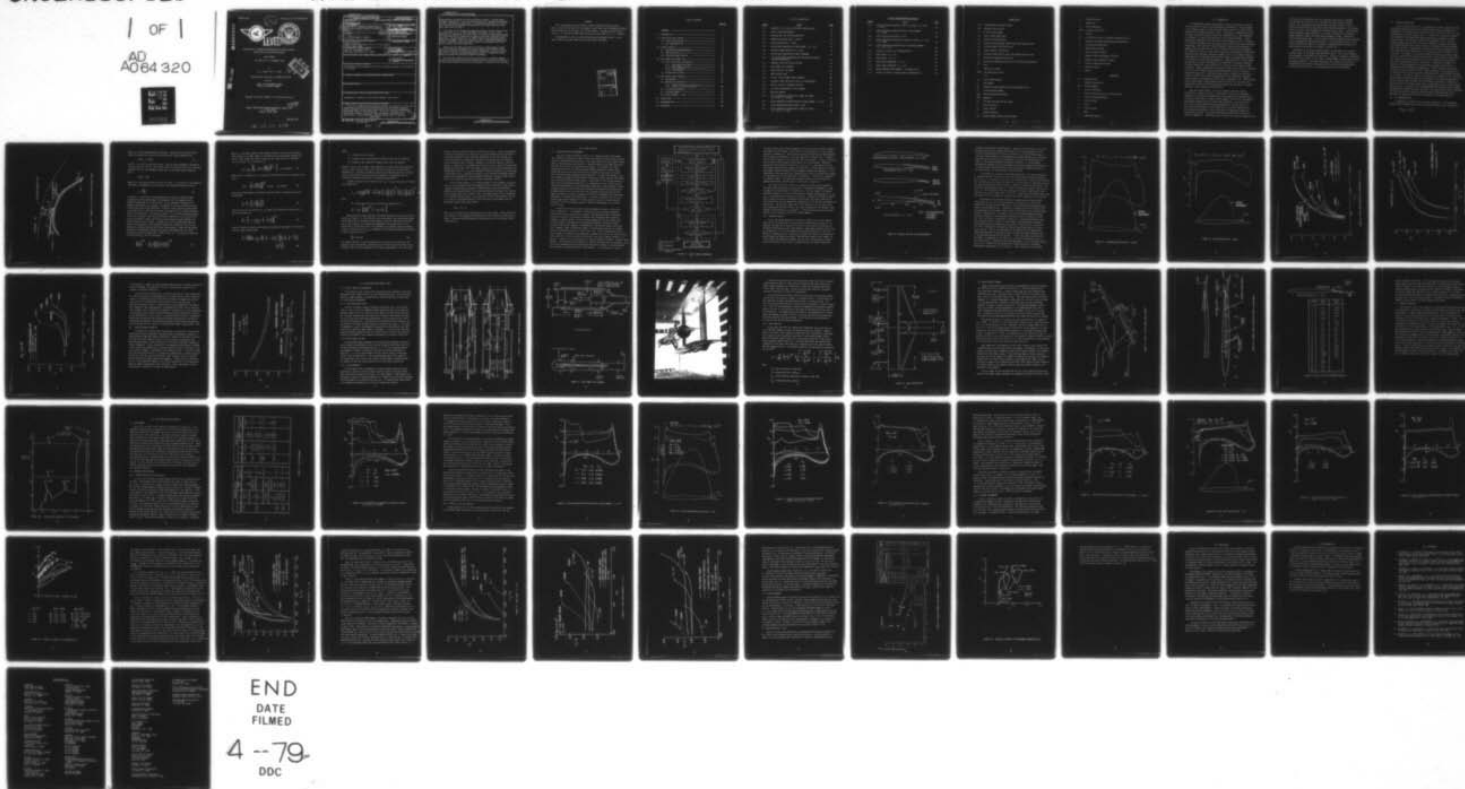


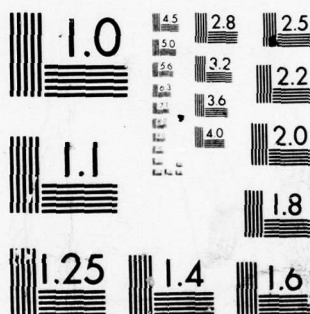
AD-A064 320

VOUGHT CORP ADVANCED TECHNOLOGY CENTER INC DALLAS TEX F/G 1/3
VALIDATION OF A TRANSONIC MANEUVER/CRUISE AIRFOIL DESIGN EMPLOY--ETC(U)
JUN 78 C H HAIGHT, R L MASK N62269-76-C-0318
ATC-B-91100/8CR-84 NADC-76047-30 NL

UNCLASSIFIED

1 OF 1
AD
A064 320





MICROCOPY RESOLUTION TEST CHART
NATIONAL BUREAU OF STANDARDS-1963-A

UNCLASSIFIED

ATC Report No. B-91100/8CR-84

ADA064320



LEVEL

VALIDATION OF A TRANSONIC MANEUVER/CRUISE AIRFOIL DESIGN
EMPLOYING ACTIVE DIFFUSION CONTROL

FINAL REPORT

(29 JUNE 1976 - 31 DECEMBER 1977)

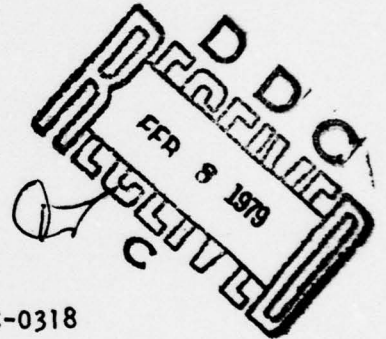
by

C. H. Haight and R. L. Mask

Prepared Under Contract No. N62269-76-C-0318

For the

NAVAL AIR DEVELOPMENT CENTER
NAVAL AIR SYSTEMS COMMAND



Approved for Public Release: Distribution Unlimited

VOUGHT CORPORATION ADVANCED TECHNOLOGY CENTER, INC.
P. O. BOX 226144
DALLAS, TEXAS 75266

389797

UNCLASSIFIED

79 02 05 046

DDC FILE COPY

17 REPORT DOCUMENTATION PAGE		READ INSTRUCTIONS BEFORE COMPLETING FORM
1. REPORT NUMBER 19 NADC-76047-30	2. GOVT ACCESSION NO.	3. RECIPIENT'S CATALOG NUMBER
4. TITLE (and Subtitle) 6 VALIDATION OF A TRANSONIC MANEUVER/CRUISE AIRFOIL DESIGN EMPLOYING ACTIVE DIFFUSION CONTROL	5. TYPE OF REPORT & PERIOD COVERED 9 FINAL REPORT. 31 29 June 1976 - December 1977	6. PERFORMING ORG. REPORT NUMBER
7. AUTHOR(s) 10 C. H./Haight and R. L./Mask	14 ATC-B-91100/8CR-84	8. CONTRACT OR GRANT NUMBER(s) 15 N62269-76-C-0318
9. PERFORMING ORGANIZATION NAME AND ADDRESS Vought Corporation Advanced Technology Center, Inc., P.O. Box 226144 Dallas, Texas 75266	10. PROGRAM ELEMENT, PROJECT, TASK AREA & WORK UNIT NUMBERS	
11. CONTROLLING OFFICE NAME AND ADDRESS Naval Air Development Center Code 6053, Warminster, Pa. 18974	12. REPORT DATE 11 23 June 1978	13. NUMBER OF PAGES 59 12, 70p
14. MONITORING AGENCY NAME & ADDRESS (if different from Controlling Office)	15. SECURITY CLASS. (of this report) Unclassified	15a. DECLASSIFICATION/DOWNGRADING SCHEDULE
16. DISTRIBUTION STATEMENT (of this Report) This document has been approved for public release and sale; its distribution is unlimited.		
17. DISTRIBUTION STATEMENT (of the abstract entered in Block 20, if different from Report)		
18. SUPPLEMENTARY NOTES		
19. KEY WORDS (Continue on reverse side if necessary and identify by block number) Aerodynamics, Transonic, Airfoil/wing, Boundary Layer Control		
20. ABSTRACT (Continue on reverse side if necessary and identify by block number) The use of advanced active diffusion control has resulted in cruise and maneuvering transonic airfoil design points which are similar enough to permit deployment from a common section while still achieving outstanding performance at both flight conditions. An airfoil thickness ratio of seven percent was selected, relating to high performance aircraft/missile applications. The antiseperation tailored contour (ATC) is the basic (continued)		

DD FORM 1 JAN 73 1473

EDITION OF 1 NOV 65 IS OBSOLETE
S/N 0102-014-6601

UNCLASSIFIED

SECURITY CLASSIFICATION OF THIS PAGE (When Data Entered)

389 797

UNCLASSIFIED

SECURITY CLASSIFICATION OF THIS PAGE(When Data Entered)

blowing/contouring device for active diffusion control. A design phase produced transonic ATC cruise and maneuvering airfoil geometries designated as TATC7C and TATC7M, respectively. Corresponding predictions of significant performance improvements motivated entry into model fabrication and wind tunnel testing tasks.)

Data taken in the Vought High Speed Wind Tunnel validate unique performance characteristics for both the TATC7C and TATC7M. At $M_{\infty} = 0.80$, increments in maneuvering lift coefficient of +0.18 and +0.40 were measured for the TATC7M section respective to supercritical and conventional airfoil baselines. Drag divergence for the TATC7C geometry was delayed by 0.08 - 0.09 on Mach number relative to predictions for a comparable Whitcomb-type section. Equivalent drag polars define potential performance gains over a wide range of operating conditions.

Because of the highly efficient ATC blowing, plenum pressure ratios in the 2-3 range are acceptable and by-pass engine bleed becomes viable. Data show ATC airfoil C_u -required, even for maneuvering, to be well within the limits of by-pass bleed and approaching levels for compressor bleed, based on estimates using existing engine technology.

The high Mach number design point performance of a variable geometry transonic section employing active diffusion control indicates the potential for unique performance and efficiency advantages in advanced airfoil design.

UNCLASSIFIED

SECURITY CLASSIFICATION OF THIS PAGE(When Data Entered)

FOREWORD

This investigation was performed by Vought Advanced Technology Center, Dallas, Texas for the Naval Air Development Center (Contract No. N62269-76-C-0318) under the auspices of the Naval Air Systems Command. The NADC contract monitor was Dr. K. T. Yen and the NASC administration was performed by Mr. R. F. Siewert.

Acknowledgments also go to Arnold Engineering Development Center for the loan of USAF wind tunnel model mounting and support equipment.

ACCESSION for	
NTIS	White Section <input checked="" type="checkbox"/>
DDC	Buff Section <input type="checkbox"/>
UNANNOUNCED	<input type="checkbox"/>
JUSTIFICATION	
BY	
DISTRIBUTION/AVAILABILITY CODES	
Dist	SPECIAL
A	

TABLE OF CONTENTS

	<u>Page No.</u>
FOREWORD -----	i
1.0 INTRODUCTION -----	1
2.0 ACTIVE DIFFUSION CONTROL -----	3
2.1 AIRFOIL APPLICATION -----	3
2.2 BLC CHARACTERISTICS -----	3
3.0 AIRFOIL DESIGN -----	9
3.1 DESIGN OBJECTIVES/PROCEDURES -----	9
3.2 TWO-POINT DESIGN -----	11
3.3 PREDICTED BLEED POTENTIAL -----	19
4.0 HIGH SPEED WIND TUNNEL TEST -----	21
4.1 FACILITY AND TEST ACCESSORIES -----	21
4.1.1 High Speed Wind Tunnel -----	21
4.1.2 Model Support System -----	21
4.1.3 Instrumentation -----	21
4.1.4 Data Reduction -----	25
4.2 DESCRIPTION OF MODELS -----	27
5.0 TEST RESULTS AND DISCUSSION -----	33
5.1 RUN SUMMARY -----	33
5.2 PRESSURE DISTRIBUTIONS -----	33
5.2.1 TATC7M Maneuvering Configuration -----	35
5.2.2 TATC7C Cruise Configuration -----	36
5.3 LIFT/DRAG PERFORMANCE -----	41
5.4 PITCHING MOMENTS -----	53
5.5 BLEED POTENTIAL - DATA -----	53
6.0 CONCLUSIONS -----	57
7.0 RECOMMENDATIONS -----	58
8.0 REFERENCES -----	59

LIST OF ILLUSTRATIONS

<u>FIGURE</u>	<u>TITLE</u>	<u>PAGE</u>
2-1	SCHEMATIC OF ATC ACTIVE DIFFUSION CONTROL DEVICE	4
3-1	AIRFOIL DESIGN PROCEDURES	10
3-2	BASELINE AND TATC SECTION GEOMETRIES	12
3-3	MANEUVERING DESIGN POINT - TATC7M	14
3-4	CRUISE DESIGN POINT - TATC7C	15
3-5	DESIGN PHASE COMPARISON OF DRAG POLARS - $M_{\infty} = 0.73$	16
3-6	REYNOLDS NUMBER EFFECT AT $M_{\infty} = 0.73$	17
3-7	DESIGN PHASE COMPARISON OF DRAG DIVERGENCE	18
3-8	FULL SPAN BLOWING CHARACTERISTICS FOR STATE-OF-THE-ART ENGINE INSTALLATION	20
4-1	TRANSONIC TEST SECTION AND EJECTOR	22
4-2	WIND TUNNEL TEST ASSEMBLY	23
4-3	MODEL INSTALLED IN TUNNEL	24
4-4	WAKE PRESSURE RAKE	26
4-5	TATC7C, 7M WIND TUNNEL MODEL ASSEMBLY	28
4-6	SCHEMATIC CROSS SECTION OF TATC7C, 7M HSWT MODELS	29
4-7	TATC7C, 7M STATIC PRESSURE ORIFICES	30
4-8	TEST SECTION BLOCKAGE OF TEST ASSEMBLY	32
5-1	HSWT RUN SUMMARY	34
5-2	TATC7M PRESSURE DISTRIBUTION AT ANGLE OF ATTACK - $M_{\infty} = 0.73, C_{\mu} = 0.0178$	35
5-3	TATC7M PRESSURE DISTRIBUTION DATA AT MACH NUMBER - $\alpha = 3.0^{\circ}$	37
5-4	TATC7M MANEUVERING DESIGN POINT - DATA	38
5-5	TATC7M PRESSURE DISTRIBUTION AT ANGLE OF ATTACK - $M_{\infty} = 0.8, C_{\mu} = 0.0161$	39

LIST OF ILLUSTRATIONS (Continued)

<u>FIGURE</u>	<u>TITLE</u>	<u>PAGE</u>
5-6	TATC7M PRESSURE DISTRIBUTION DATA AT BLOWING - $M_{\infty} = 0.8$, $\alpha = 3.0^{\circ}$	40
5-7	TATC7C PRESSURE DISTRIBUTION DATA AT MACH NUMBER - $C_{\mu} = 0.005$	42
5-8	TATC7C CRUISE DESIGN POINT - DATA	43
5-9	TATC7C PRESSURE DISTRIBUTION AT ANGLE OF ATTACK - $M_{\infty} = 0.9$, $C_{\mu} = 0.005$	44
5-10	TATC7C PRESSURE DISTRIBUTION DATA AT REYNOLDS NUMBER - $M_{\infty} = 0.9$, $\alpha = 4^{\circ}$	45
5-11	TATC7M, 7C AIRFOIL LIFT CHARACTERISTICS	46
5-12	DRAG POLARS - $M_{\infty} = 0.8$	48
5-13	DRAG POLARS - $M_{\infty} = 0.9$	50
5-14	CRUISE DRAG DIVERGENCE - $C_{\ell} = 0.4$	51
5-15	CRUISE DRAG DIVERGENCE - $C_{\ell} = 0.6$	52
5-16	DRAG DIVERGENCE MACH NUMBER vs. THICKNESS RATIO	54
5-17	TATC7M, 7C AIRFOIL PITCHING MOMENT CHARACTERISTICS	55

NOMENCLATURE

ATC	Antiseparation Tailored Contour
BLC	Boundary Layer Control
c	Airfoil Chord Length
C_d	Section Drag Coefficient
C_l	Section Lift Coefficient
C_m	Section Pitching Moment Coefficient About Quarter Chord
C_N	Section Normal Force Coefficient
C_p	Local Pressure Coefficient
C_p^*	Pressure Coefficient at Local Mach Number equal to one
C_μ	Blowing Jet Momentum Coefficient
$C_{\mu c}$	Blowing Jet Momentum Coefficient For Complete Energization
D	Drag
h	Blowing Slot Width
HSWT	High Speed Wind Tunnel
L	Lift
L_M	Mixing Ramp Distance
M	Mach Number
\bar{M}_j	Blowing Jet Mach Number Attained By Expanding To P_∞
M_∞	Freestream Mach Number
M_{DD}	Drag Divergence Mach Number
Mom	Momentum
\dot{m}_j	Jet Mass Flow Rate Per Unit Span
P	Static Pressure
P_o	Total Pressure
q	Dynamic Pressure
Re_c	Reynolds Number Based on Chord Length

79 02 03 040

s	Surface Distance
T	Temperature
T _o	Total Temperature
TATC	Transonic ATC Airfoil
U	Velocity
\bar{V}_j	Jet Velocity Attain by Isentropic Expansion to P _∞
x	Distance from Leading Edge Measured Along Chord
z	Distance Along Wake Rake
α	Model Angle of Attack
γ	Ratio of Specific Heats
δ*	Boundary Layer Displacement Thickness
θ	Boundary Layer Momentum Thickness
$\bar{\theta}$	Effective Momentum Thickness
λ	Empirical Factor
ρ	Density

SUBSCRIPTS

bl	Boundary Layer
c	Complete Energization
DD	Drag Divergence
j	Jet Exit Conditions
L	External Conditions at Lip of Blowing Slot
o	Total Pressure/Temperature
R	Diffusion Ramp
T	Total
vl	Viscous Losses
w	Wake
∞	Freestream Condition

1.0 INTRODUCTION

Two fundamental problems encountered by tactical aircraft or missiles during transonic flight are drag divergence and buffeting. Drag divergence is the sudden increase in drag with Mach number caused by increasing shock strengths and thickening boundary layers. Buffeting is associated with the unsteady interaction between a shock and a separated flow. Both phenomena are related to critical flow conditions on the lifting surfaces. Cruise performance, measured by the transonic cruise parameter $M_{\infty} L/D$, is improved by increasing the Mach number attainable without entering the drag divergence regime (M_{DD} - Mach number of drag divergence). Maneuvering performance is dependent on the upper limit of the lift coefficient that can be obtained, with admissible levels of drag, before separation and subsequent buffet onset. Decreasing wing thickness, optimizing aspect ratio, and increasing leading edge sweep help to attenuate adverse shock effects but these passive methods are limited as to what they can accomplish. Advanced airfoil section design epitomized by the work of Whitcomb (e.g., Reference 1) has been successful for point designs but lacks flexibility in covering a full range of flight conditions. Camber requirements are normally conflicting in terms of designing a single airfoil capable of near-optimum performance at both cruise and maneuvering conditions. Blowing has been used as an add-on to a variety of transonic airfoils to achieve high maneuvering lift coefficients through supercirculation and separation control (e.g., References 2,3). These studies utilize conventional blowing devices such as the wall jet, jet flap, etc. and generally suffer from high bleed requirements and the lack of a unified approach to blown transonic airfoil design.

Under the present effort, the use of advanced diffusion control, validated for transonic sections in Reference 4, along with a deployment commonality constraint has produced cruise and maneuvering configuration design points that define a single variable geometry airfoil with outstanding performance characteristics at both flight conditions. An airfoil thickness ratio of seven percent was selected because of the past attention given to thicker sections (11-12%, Reference 1,4) and the immediate need for innovative techniques in the thinner airfoil range more suitable to fighter type aircraft. The cruise and maneuvering design points have exceptional commonality: performance data indicate that required changes can be

limited to small deflections over the last 25% of the airfoil, compared with changes over 50% chord for an analogous Whitcomb two-point design. Further, the integrated contouring/blowing techniques inherent in active diffusion control lead to practicable engine bleed requirements. The primary device utilized is the antiseparation tailored contour (ATC). The ATC device controls boundary layer separation and provides a mechanism for replacing gradual geometric camber with localized jet/geometry camber, effectively varying with blowing rate. In this process, efficient boundary layer energization is coupled with rapid flow diffusion. Active diffusion control is discussed in Section 2.0 and its utilization in maneuvering/cruise design of a seven percent thick airfoil is treated in Section 3.0.

Validation of the airfoil design concept was obtained in a series of transonic tests in the Vought High Speed Wind Tunnel. Facilities, hardware, and procedures are described in Section 4.0. Section 5.0 contains a discussion of airfoil data in terms of lift, drag, pitching moment, pressure distribution, and blowing momentum. The report concludes with a summary of results and recommendations for detailing advanced airfoil options and incorporation of the section characteristics in three-dimensional wing configurations.

2.0 ACTIVE DIFFUSION CONTROL

2.1 AIRFOIL APPLICATION

Active diffusion control is a new approach to solving transonic airfoil problems and has the potential for improving both cruise and maneuvering performance. The primary device utilized for active diffusion control is the antiseparation tailored contour (ATC). It consists of an auxiliary blowing slot upstream of a contoured BLC energization zone, followed by a severe diffusion step. The concept is based on the hypothesis that if the mainstream boundary layer existing at the slot location is properly energized, significant diffusion over a short distance is possible. Efficient boundary layer energization in combination with rapid flow diffusion relaxes the airfoil shape constraints and permits a tailoring of the airfoil pressure distribution. For example, an aft upper surface ATC device can produce a near-critical "roof-top" distribution extending over ninety percent of the airfoil, thus reducing the shock strengths for a given loading while simultaneously controlling aft separation (e.g., Figure 3-4). Effective aft camber is a function of blowing, especially on the thinner sections, which assists in minimizing cruise-to-maneuvering deployment. The ATC principle can also be utilized for the tailoring of airfoil pitching moments. A key characteristic of the ATC device is the low auxiliary blowing rate (or engine bleed) required for full BLC. This permits the use of relatively low pressure fan air for bleed without having prohibitive mass flow requirements. The transonic approach to active diffusion control began with the concept investigation in Reference 5 and was verified in the wind tunnel tests of Reference 4 using a twelve percent thick section. It evolved from a high technology STOL concept that has already undergone Navy-funded wind tunnel testing.⁶ The transonic ATC airfoil, therefore, has inherent qualities related to high performance STOL operation and the potential for producing an aircraft with superior all-around capability.

2.2 BLC CHARACTERISTICS

A schematic of the ATC device is shown in Figure 2-1. The mainstream boundary layer momentum loss at the lip of the ATC blowing slot is defined as

$$(\text{Mom})_{b\ell} = (\rho \theta U^2)_L$$

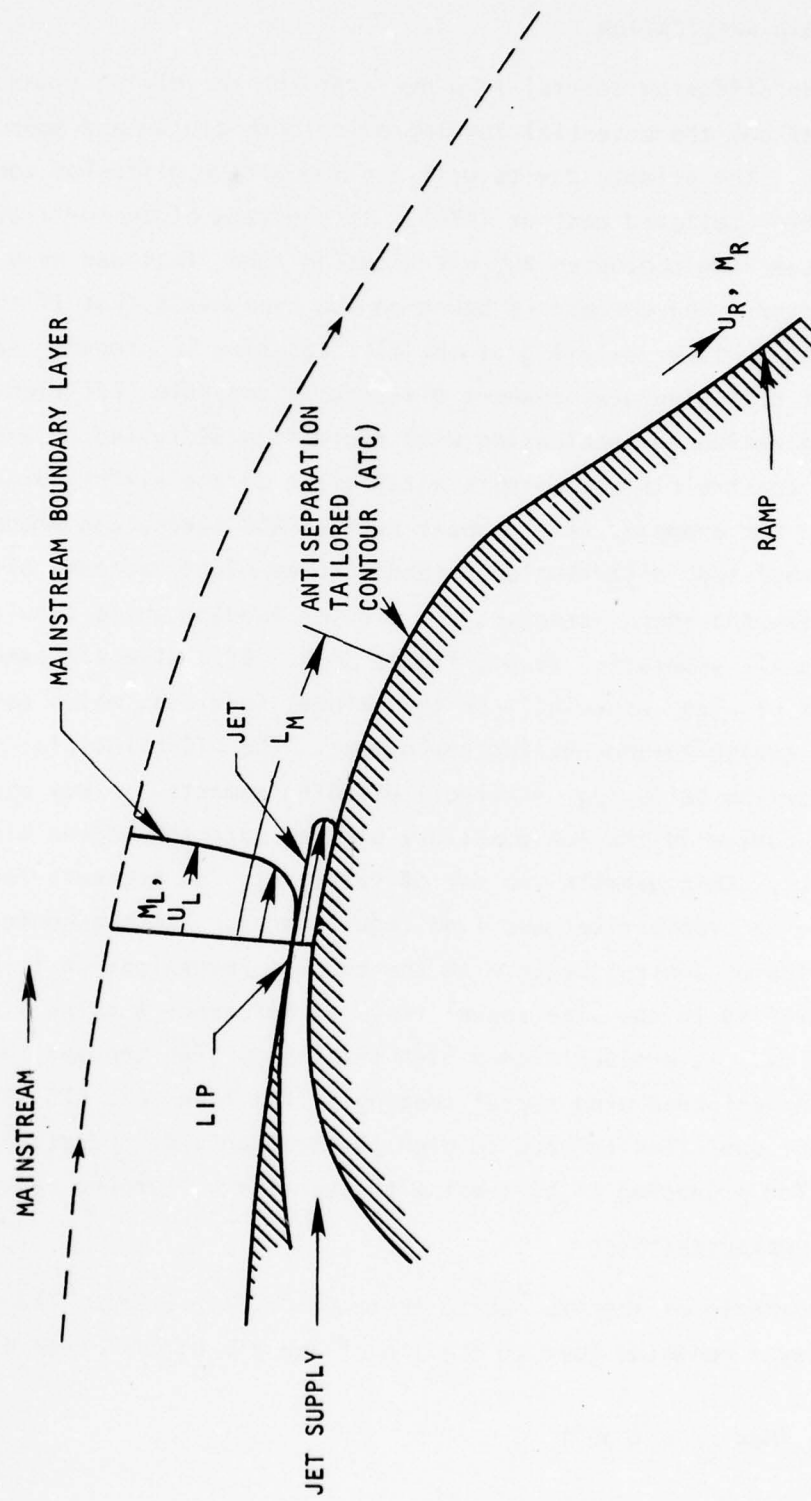


FIGURE 2-1 SCHEMATIC OF ATC ACTIVE DIFFUSION CONTROL DEVICE

where θ_L is the incoming momentum thickness. Experience with the ATC device leads to an empirical relation for the effective viscous momentum loss;

$$(\text{Mom})_{v\ell} = (\rho \bar{\theta} U^2)_L \quad (1)$$

with $\bar{\theta}_L = \lambda \theta_L$ and λ an empirical factor. The jet supply momentum is defined as the jet mass flow times \bar{V}_j , the velocity which the jet would attain by isentropic expansion from the jet stagnation conditions to freestream static pressure.

Thus,

$$(\text{Mom})_j = \dot{m}_j \bar{V}_j$$

where \dot{m}_j is the total jet mass flow per unit span. In the form of a jet momentum coefficient, referenced to airfoil chord c and freestream dynamic pressure,

$$C_\mu = \frac{\dot{m}_j \bar{V}_j}{q_\infty c} \quad (2)$$

In general, C_μ can be any value depending on the amount of boundary layer energization desired and becomes interdependent with the momentum deficit appearing downstream of the ATC device. The jet momentum coefficient for complete energization C_{μ_c} , however, corresponds to a zero θ condition leaving the BLC region and can be predicted. A control volume analysis has been used to estimate the C_{μ_c} required for complete energization of an incoming boundary layer by a blowing jet. The analysis assumes: (1) a uniform external pressure field, (2) isentropic flow, (3) uniform total temperature, (4) a uniform flow exiting the control volume, and (5) that the mainstream losses dominate the newly-building ATC wall losses. Although this control volume model does not permit the calculation of the distance required for completion of the mixing process nor velocity profiles within the mixing region, it does provide usable estimates of compressible blowing requirements and handles ATC wall losses secondarily through the empirical λ factor in Eq. (1). The essential equations for calculating C_{μ_c} are the following.

$$\left(\frac{P_{Oj}}{P_{O\infty}} \right)^{\frac{\gamma-1}{\gamma}} = \left(\frac{1 + \frac{\gamma-1}{2} M_j^2}{1 + \frac{\gamma-1}{2} M_L^2} \right) \left(\frac{P_j}{P_L} \right)^{\frac{\gamma-1}{\gamma}} \quad (3)$$

Here, M_L is the Mach number of the external stream at the lip of the blowing slot, and M_j is the Mach number at the opening of the convergent blowing slot and is, thus, always less than or equal to one. When the jet is unchoked, $P_j = P_L$, and Eq. (3) is solved for M_j .

$$M_j^2 = \frac{2}{\gamma-1} \left[\left(1 + \frac{\gamma-1}{2} M_L^2 \right) \left(\frac{P_{Oj}}{P_{O\infty}} \right)^{\frac{\gamma-1}{\gamma}} - 1 \right], \text{ jet unchoked} \quad (4)$$

When the jet is choked, $M_j = 1$, and Eq. (3) may be solved for the pressure ratio P_j/P_L .

$$P_j/P_L = \left(\frac{1 + \frac{\gamma-1}{2} M_L^2}{1 + (\gamma-1)/2} \right)^{\frac{\gamma}{\gamma-1}} P_{Oj}/P_{O\infty}, \text{ jet choked} \quad (5)$$

Once the jet Mach number and pressure ratio are known, the density ratio can be obtained.

$$\frac{\rho_j}{\rho_L} = \frac{P_j}{P_L} \left(\frac{1 + \frac{\gamma-1}{2} M_j^2}{1 + \frac{\gamma-1}{2} M_L^2} \right) \quad (6)$$

Then the ratio of jet velocity, U_j , to velocity of external stream at the lip may be calculated via

$$\frac{U_j}{U_L} = \left[1 + \frac{2}{(\gamma-1)M_L^2} \left(1 - \frac{P_j}{P_L} \frac{\rho_L}{\rho_j} \right) \right]^{1/2} \quad (7)$$

From the integral continuity and momentum conservation equations for the mixing control volume, one can show

$$\frac{\bar{\theta}_L}{h} = \left(\frac{\bar{\theta}_L}{c} \right) \left(\frac{c}{h} \right) = \frac{1}{\gamma M_L^2} \left(\frac{P_j}{P_L} - 1 \right) + \frac{\rho_j}{\rho_L} \frac{U_j}{U_L} \left[\left(\frac{U_j}{U_L} - 1 \right) \left(1 - \frac{2\delta_j^*}{h} \right) - \frac{U_j}{U_L} \frac{2\theta_j}{h} \right], \quad (8)$$

where

h = blowing jet slot width,

δ_j^* = boundary layer displacement thickness within the slot opening,

θ_j = boundary layer momentum thickness within the slot opening.

Usually, the jet slot boundary layer parameters are specified along with $\bar{\theta}_L/c$, M_L and a total pressure ratio so Eq. (8) may be solved for the slot width parameter h/c . Equations (3)-(8) provide all the necessary auxiliary information to calculate the various terms which appear in the equation for the required jet momentum coefficient for complete energization.

Standard isentropic flow formulas with $T_{0j} = T_{0\infty}$ and inclusion of internal slot losses give

$$C_{\mu_c} = 2 \frac{\rho_j}{\rho_L} \left(\frac{h}{\bar{\theta}_L} \right) \left(\frac{\bar{\theta}_L}{c} \right) \left(1 - \frac{2\delta_j^*}{h} \right) \frac{M_j}{M_\infty} \left(\frac{1 + \frac{\gamma-1}{2} M_\infty^2}{1 + \frac{\gamma-1}{2} M_j^2} \right)^{1/2} \frac{\bar{M}_j}{M_\infty} \left(\frac{1 + \frac{\gamma-1}{2} M_\infty^2}{1 + \frac{\gamma-1}{2} \bar{M}_j^2} \right)^{1/2} \quad (9)$$

where

\bar{M}_j = Mach number blowing jet attains by expanding to P_∞ ,

$$\bar{M}_j^2 = \frac{2}{\gamma-1} \left[\left(\frac{P_{0j}}{P_{0\infty}} \right)^{\frac{\gamma-1}{\gamma}} \left(1 + \frac{\gamma-1}{2} M_\infty^2 \right) - 1 \right]$$

Determination of other pertinent ATC design parameters such as the mixing length L_M (Figure 2-1), the diffusion ratio constraints, and the jet/mainstream mixing angle follow from empiricisms based on a mass of experimental ATC data. The mixing length L_M is configuration dependent in the sense that, at the design point, mixing must occur in the absence of an adverse pressure gradient. Further, the empiricism for L_M is dependent on the mainstream momentum thickness at the lip and has the form

$$\frac{L_M}{\bar{\theta}_L} = \text{constant} \quad (10)$$

This means iteration is required between the inviscid airfoil solution, the boundary layer calculations, and the location of both the blowing slot and the diffusion step to insure compatibility of the L_M requirements. The flow chart

given in the next section further illustrates this point. Since the hypothesis (verified by experiment) is that after L_M the mainstream has been restored to an effective potential flow condition, attachment of the flow through the diffusion process is insured and the pressure distribution can be predicted by the inviscid airfoil solution. Nominally, for design purposes a value of $M_L/M_R = 2$ (Figure 2-1) corresponds empirically to the $C_{\mu C}$ level of energization. Because of the current lack of reliable transonic wall jet mixing analyses, the underblowing case of $C_{\mu} < C_{\mu C}$ was treated by scaling the amount of θ_L energized by the factor $C_{\mu}/C_{\mu C}$, carrying the excess θ_L loss through the imposed pressure gradient, and determining the corresponding non-zero θ leaving the BLC region. This in turn modified the effective camber produced by the ATC.

For jet engine bleed, C_{μ} is a basic parameter in the drag/BLC evaluation since it can be combined with the aerodynamic drag coefficient C_d and directly related to engine-wing performance. Bleed effects on engine performance depend on the characteristics of the total BLC/propulsion system, most notably on the required auxiliary pressure ratio, the bleed location (fan or compressor air), and BLC ducting losses. For a simple BLC airfoil configuration, the jet C_{μ} is the only available measure of auxiliary blowing requirements and the equivalent section drag $(C_d)_T$ becomes

$$(C_d)_T = C_d + C_{\mu}$$

where C_d is the wake drag as detected by a wake rake survey. Those definitions will be used in all subsequent determinations of ATC transonic airfoil performance. Practical available-required bleed matchups will be discussed further in Section 3.3.

3.0 AIRFOIL DESIGN

3.1 DESIGN OBJECTIVES/PROCEDURES

The use of active diffusion control in a transonic airfoil environment was validated in Reference 4 under controlled conditions which dictated utilization of a conventional fore-contour (C-141 type) mated with an aft upper surface ATC on a twelve percent thick section. Detailed baseline test data were available for this initial ATC performance evaluation. The present ATC airfoil design objectives are to combine advanced leading edge/lower surface design principles with an aft upper surface ATC to produce unique levels of design point roof-top loading and maximized performance. For specified design C_{ℓ} , M_{∞} , this reduces the peak local Mach number relative to non-ATC sections and further acts to reduce off-design shock effects. Application of this design concept to both cruise and maneuvering design C_{ℓ} , M_{∞} combinations, while restricting the resulting two geometries to have deployment commonality, then produces a single variable geometry airfoil design with improved cruise/maneuvering performance. Whitcomb supercritical sections with their shockless fore-contouring and aft camber and the ATC results of Reference 4 provide the necessary high technology references for accomplishing the design. An airfoil thickness ratio of seven percent was selected because of the past attention given to thicker sections (11-12%),^{1,4} and the immediate need for innovative techniques in the thinner airfoil range.

An outline of the ATC airfoil design procedures is given in flow chart form in Figure 3-1. It represents a unified view of the transonic analyses, the ATC empiricisms, and the BLC simulation techniques described in References 4,5 and in Section 2.0 and serves to define the interactions and iterations inherent in the ATC design. After the design objectives are set (Figure 3-1), inviscid transonic calculations are performed through an iterative process⁵ to specify the airfoil geometry corresponding to the desired pressure distribution. Boundary layer calculations predict θ distributions and test for separation for the passive portions of the airfoil flow. The ATC energization and diffusion region is assumed to have completely attached flow and to have blowing levels set to maintain but not to perturb the pressure distribution except through δ^* reduction. A second inviscid calculation is then performed to include δ^* boundary layer effects. These transonic calculations are coupled, when feasible, by automatic iteration of the Garabedian and Korn program as modified by Jameson to include boundary layer effects (corrected drag form - GKJ Program). It is important to note at

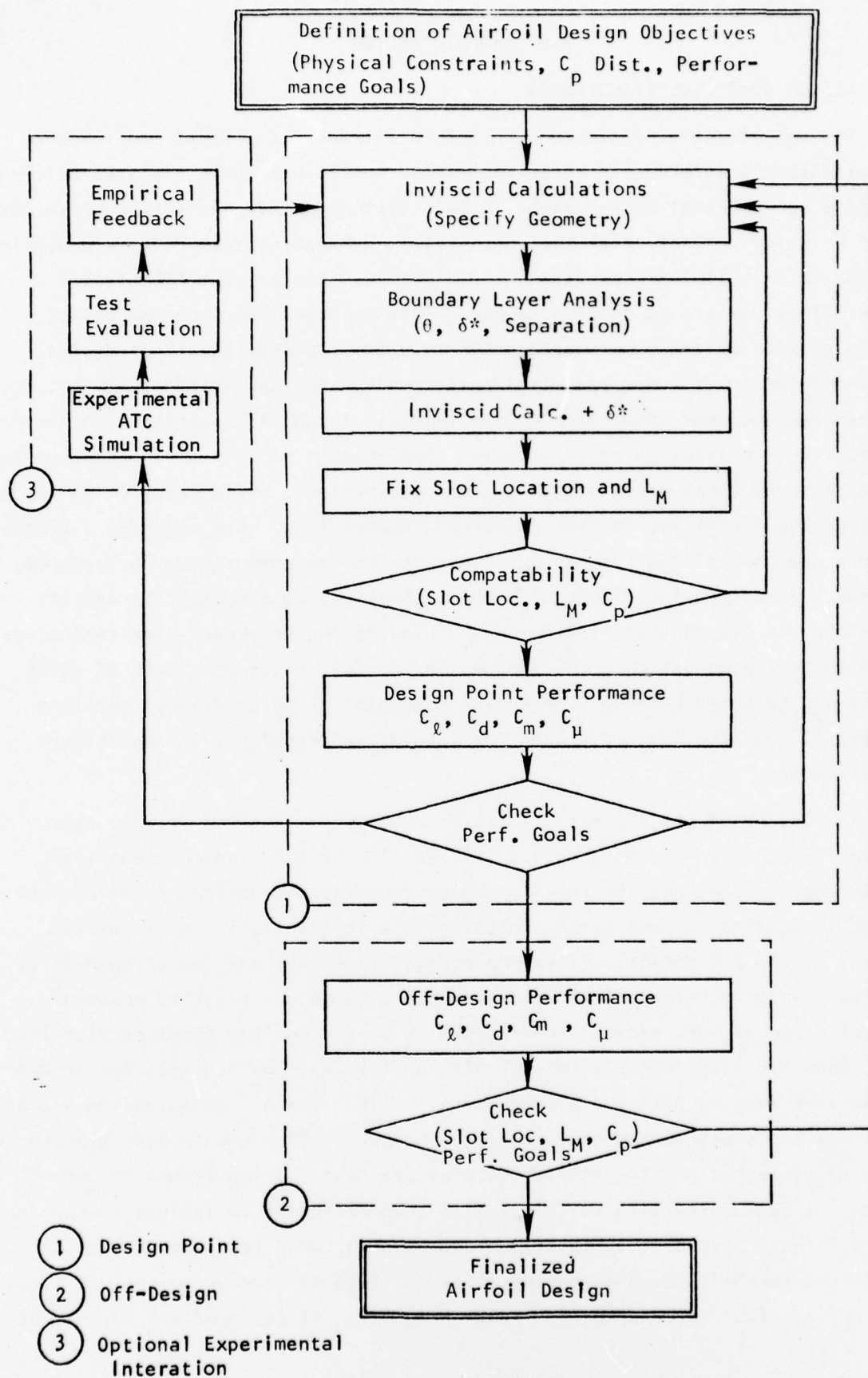


FIGURE 3-1 AIRFOIL DESIGN PROCEDURES

this point that, within these assumptions, the pressure distribution includes the effects of ATC blowing. Verification of the assumptions is given experimentally in Reference 4. The next step locates the blowing slot and determines the available L_M according to the rules described in Section 2.2. A compatibility check is made to insure that Eq. (10) is satisfied. If not, an iteration back to the inviscid geometry specification must be performed. Otherwise, design point performance in terms of C_ℓ , C_d , C_m , C_μ is calculated utilizing GJK Program output and the methods of Section 2.2. A check against the performance goals determines whether further geometry changes are required. If the experimental data base needs more substantiation, a BLC simulation test program is undertaken such as that described in Reference 4. This was not required in the present effort. The above tasks complete the ATC airfoil design point geometry/performance specifications as outlined in Figure 3-1.

The impact of the ATC airfoil on transonic aircraft design depends on the design point advantages carrying over to off-design improvements in drag divergence and buffet onset lift coefficient. The last stage in the design procedures (Figure 3-1) involves off-design performance calculations of C_ℓ , C_d , C_m , C_μ , and comparisons with the pre-set goals. Because the off-design operation includes moving and strengthening shock waves, the local conditions at the blowing slot are also checked for compatibility with the ATC requirements of Section 2.2. The empirical data base for the blowing is for a sub-critical local freestream flow and, further, the shock thickening of the boundary layer changes the requirement on L_M through θ_L . Off-design operation can therefore require a final iteration on the ATC airfoil geometry.

3.2 TWO-POINT DESIGN

As per the design objectives discussed in Section 3.1, airfoil design tasks led to the definition of a two-point cruise/maneuvering design for an advanced 7 percent thick transonic ATC (TATC) airfoil and the calculation of off-design characteristics for each geometry. Deployment commonality was used as a constraint. The two ATC geometries, designated TATC7C for cruise and TATC7M for maneuvering, are illustrated in Figure 3-2 along with conventional⁷ and Whitcomb type baseline sections. Both Whitcomb supercritical shapes, for cruise (SC7C) and maneuvering (SC7M), evolved from a 1976 analytical design study for 6 percent thick airfoils conducted jointly by Vought Engineering

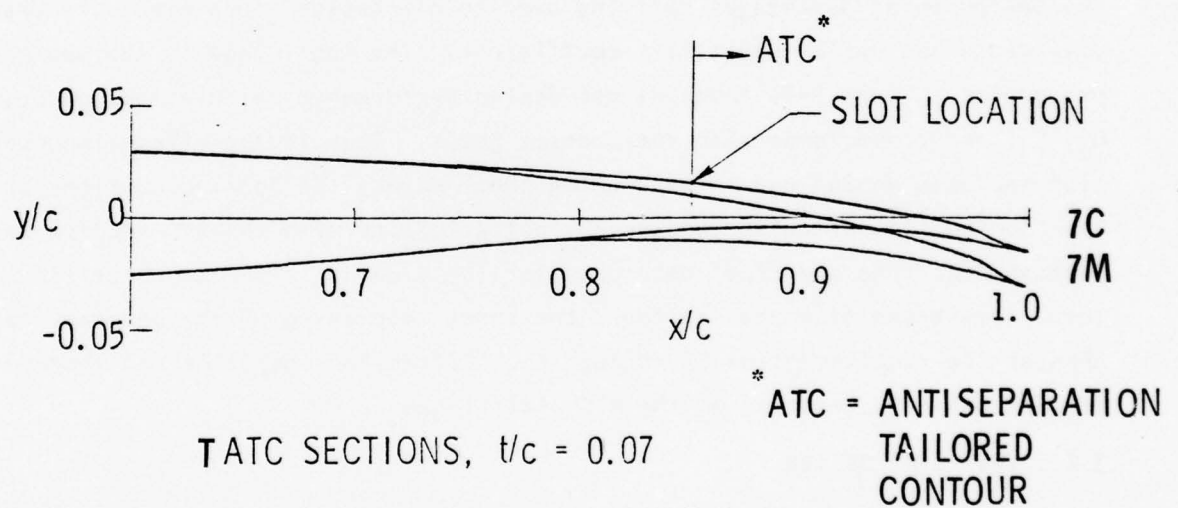
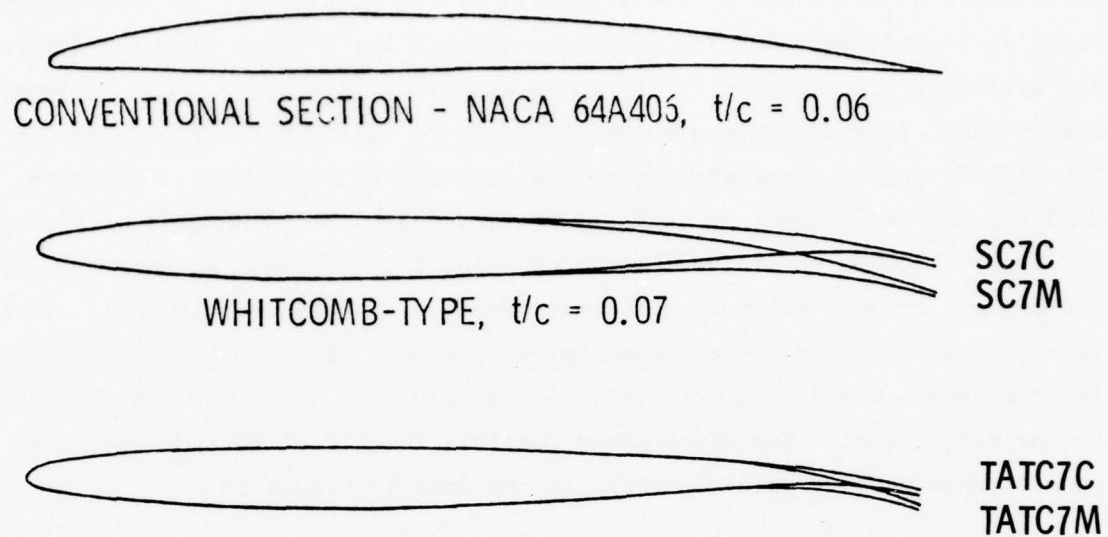


FIGURE 3-2 BASELINE AND TATC SECTION GEOMETRIES

personnel and Whitcomb at NASA-Langley. Expansion of the airfoils to a seven percent thickness has produced what should be a very representative "thin" airfoil Whitcomb baseline for the ATC comparison. Active diffusion control principles have enabled the cruise/maneuvering camber changes to be limited to small deflections over the last 25 percent of the airfoil (blowing slot at 0.85 c), thus making deployment commonality feasible. If the analogous Whitcomb-type geometries were considered as cruise and maneuvering settings for a single variable geometry section, significant camber changes would have to be effected over the last 50 percent of the airfoil.

The TATC7M, 7C sections were designed analytically for best performance at maneuvering (max. roof-top C_{ℓ}) and cruise (minimized drag) points defined by $M_{\infty} = 0.73$, $C_{\ell} = 1.47$ and $M_{\infty} = 0.8$, $C_{\ell} = 0.6$, respectively. Pressure distributions for these two cases are given in Figures 3-3, 3-4 and clearly illustrate the roof-top loading associated with ATC airfoils. Design C_{μ} values are also noted. Calculations were performed at $Re_c = 10 \times 10^6$ as a compromise between lower values ($2.5 - 6 \times 10^6$) associated with the subsequent wind tunnel testing and flight conditions that could range to $Re_c = 60 \times 10^6$. Analytical performance checks were made over the full Re_c range for selected cases after completion of the designs.

Performance at design and off-design is summarized in Figures 3-5,6,7. Drag polars (C_{ℓ} vs. $C_d + C_{\mu}$) are plotted in Figure 3-5 for $M_{\infty} = 0.73$ and comparisons are made with calculations for the 7 percent Whitcomb baseline and data for the 64A406 section. Increments in maneuvering lift of 0.18 and 0.50 are predicted, with equivalent drag, relative to Whitcomb-type and conventional airfoils, respectively. The behavior of the ATC variable geometry/blowing envelope in Figure 3-5 was projected analytically over the range $2.5 \times 10^6 \leq Re_c \leq 60 \times 10^6$ and is illustrated in Figure 3-6. Predicted performance gains carry through the full tunnel to flight range. Drag divergence comparisons for nominal blowing off conditions are plotted in Figure 3-7 at C_{ℓ} levels of 0.4, 0.6. Blowing-on ATC predictions show no significant benefits at these low C_{ℓ} levels. Clearly, the deployment of the TATC7C from the maneuvering TATC7M configuration is required to match the drag divergence characteristics of the Whitcomb-type SC7C cruise section. In fact the predictions show that the TATC7C is comparable to the SC7C at $C_{\ell} = 0.6$ and slightly better at $C_{\ell} = 0.4$ (Figure 3-7). In addition, the TATC7C deployment, at the low design blowing level of $C_{\mu} = 0.0017$, has the potential for producing distinct off-design performance improvements at $M_{\infty} = 0.8$ for $C_{\ell} > 0.6$, relative to the Whitcomb

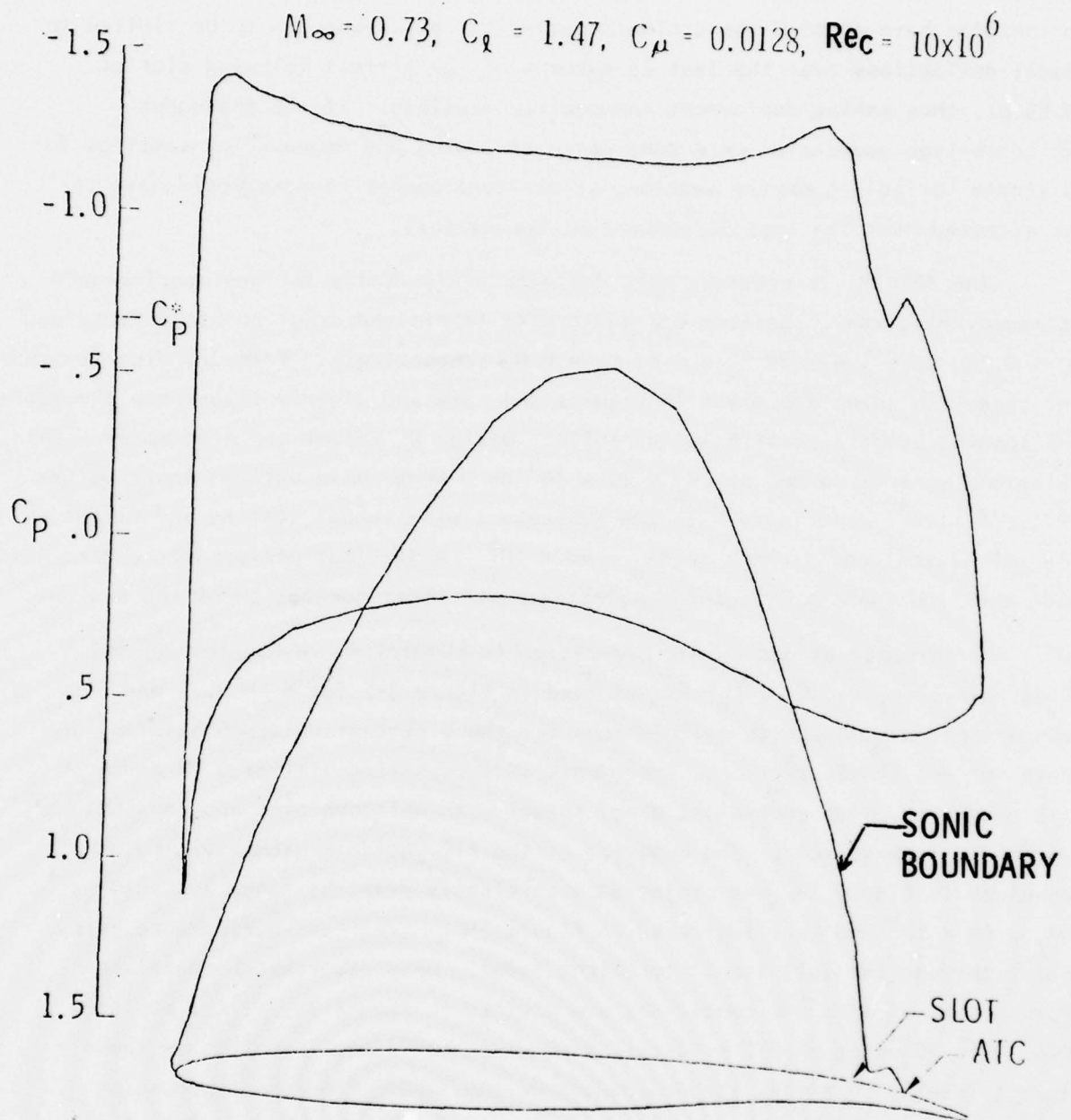


FIGURE 3-3. MANEUVERING DESIGN POINT - TATC7M

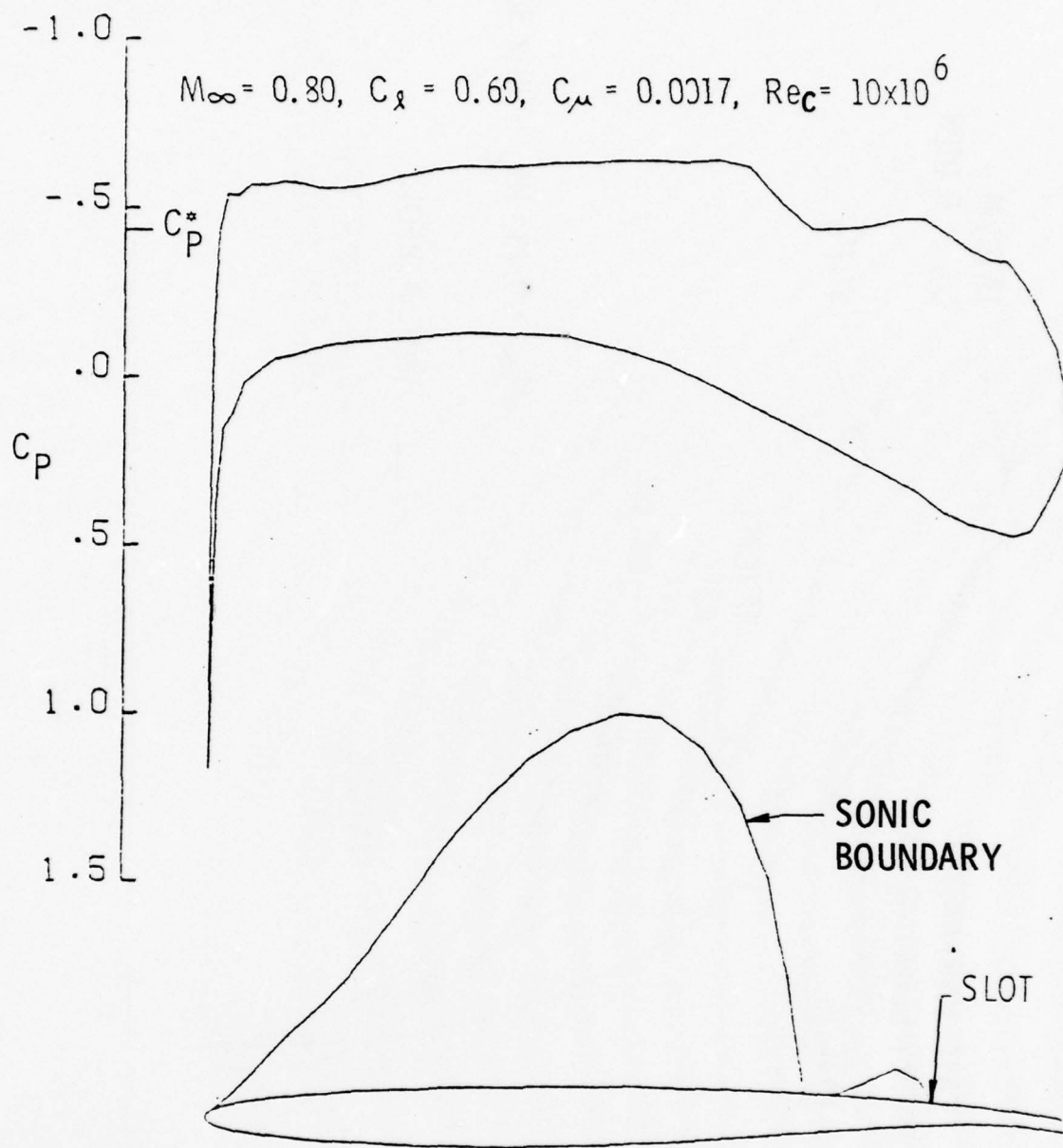


FIGURE 3-4 CRUISE DESIGN POINT - TATC7C

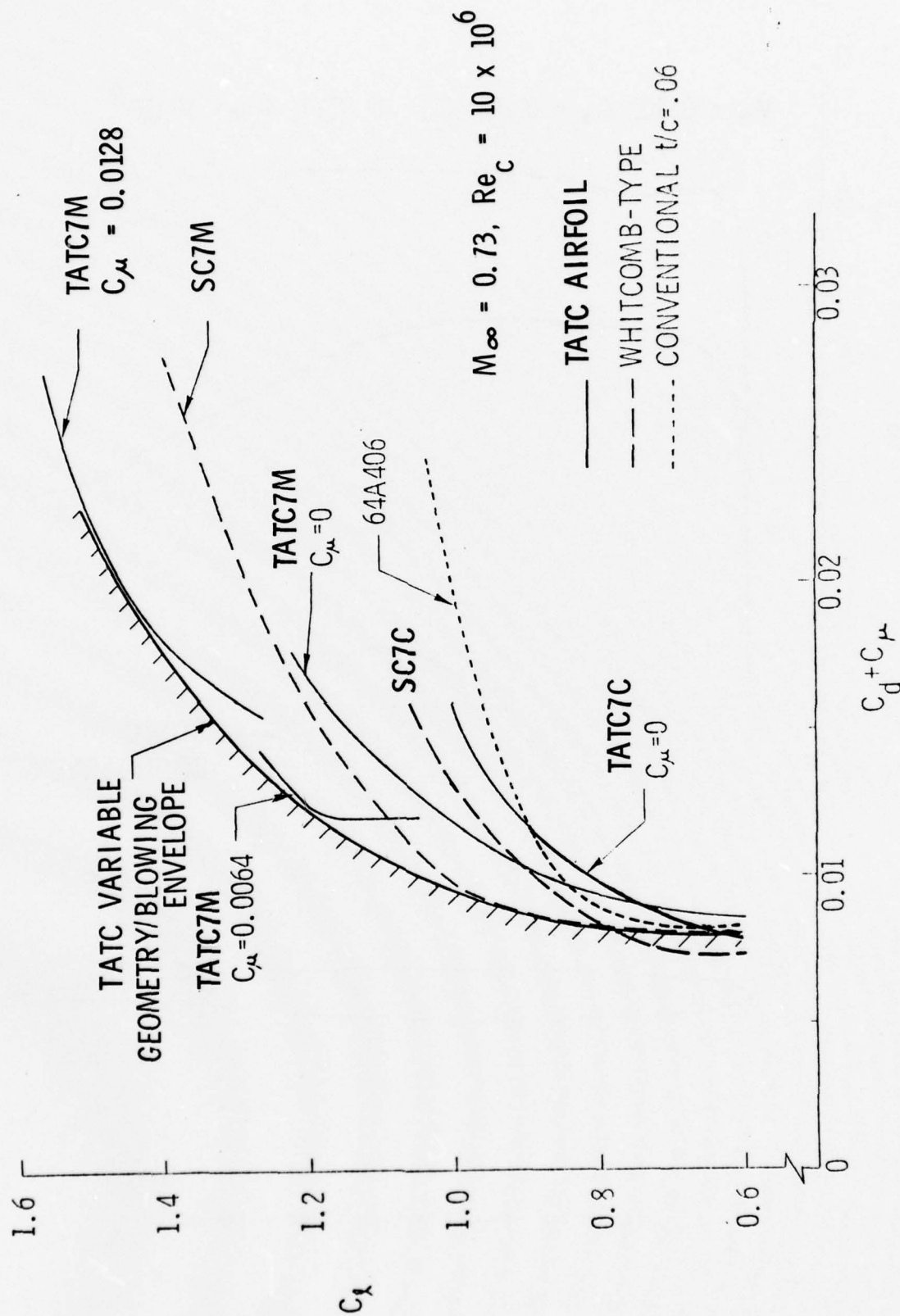


FIGURE 3-5 DESIGN PHASE COMPARISON OF DRAG POLARS - $M_\infty = 0.73$

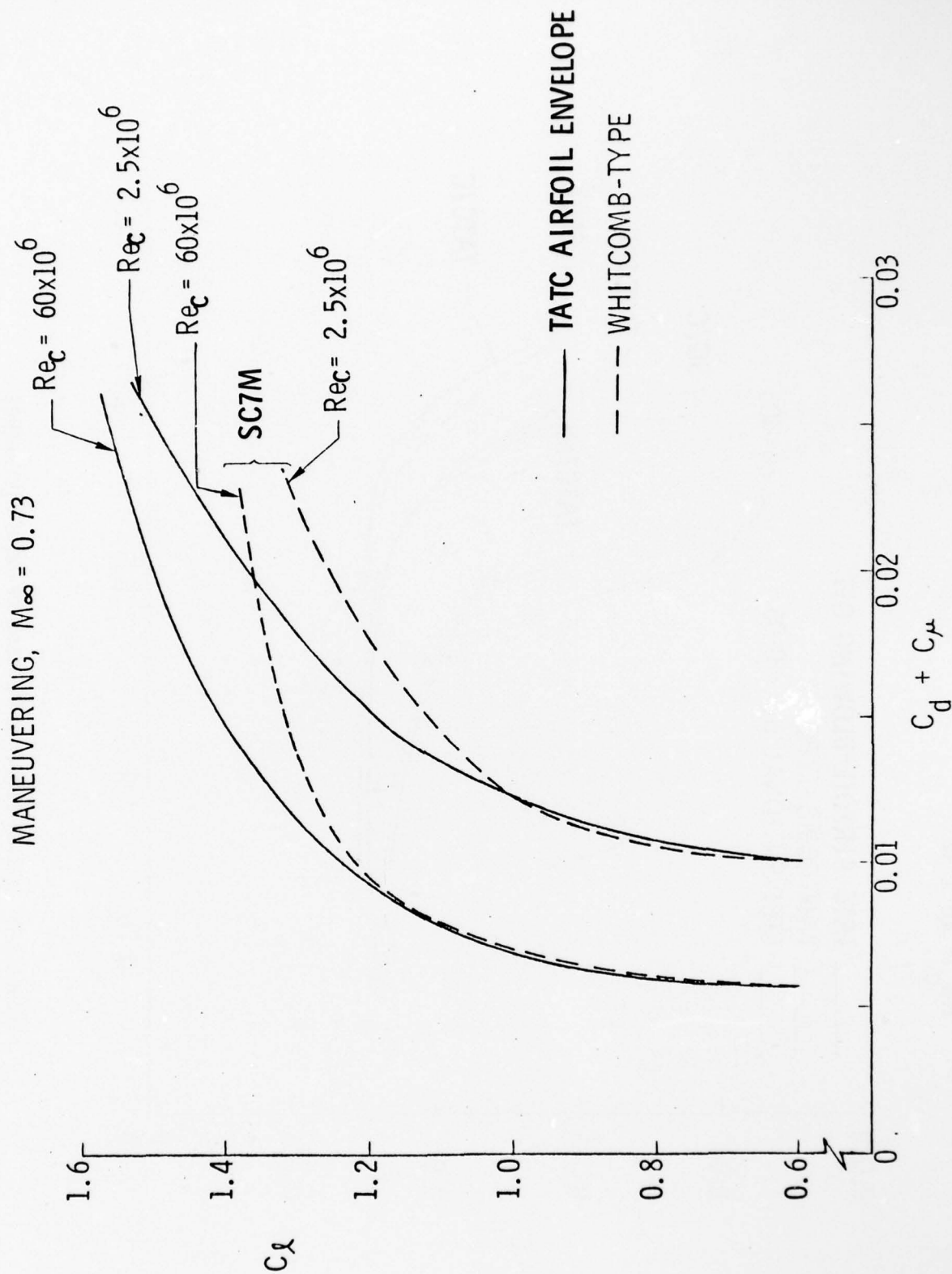


FIGURE 3-6 REYNOLDS NUMBER EFFECTS AT $M_\infty = 0.73$

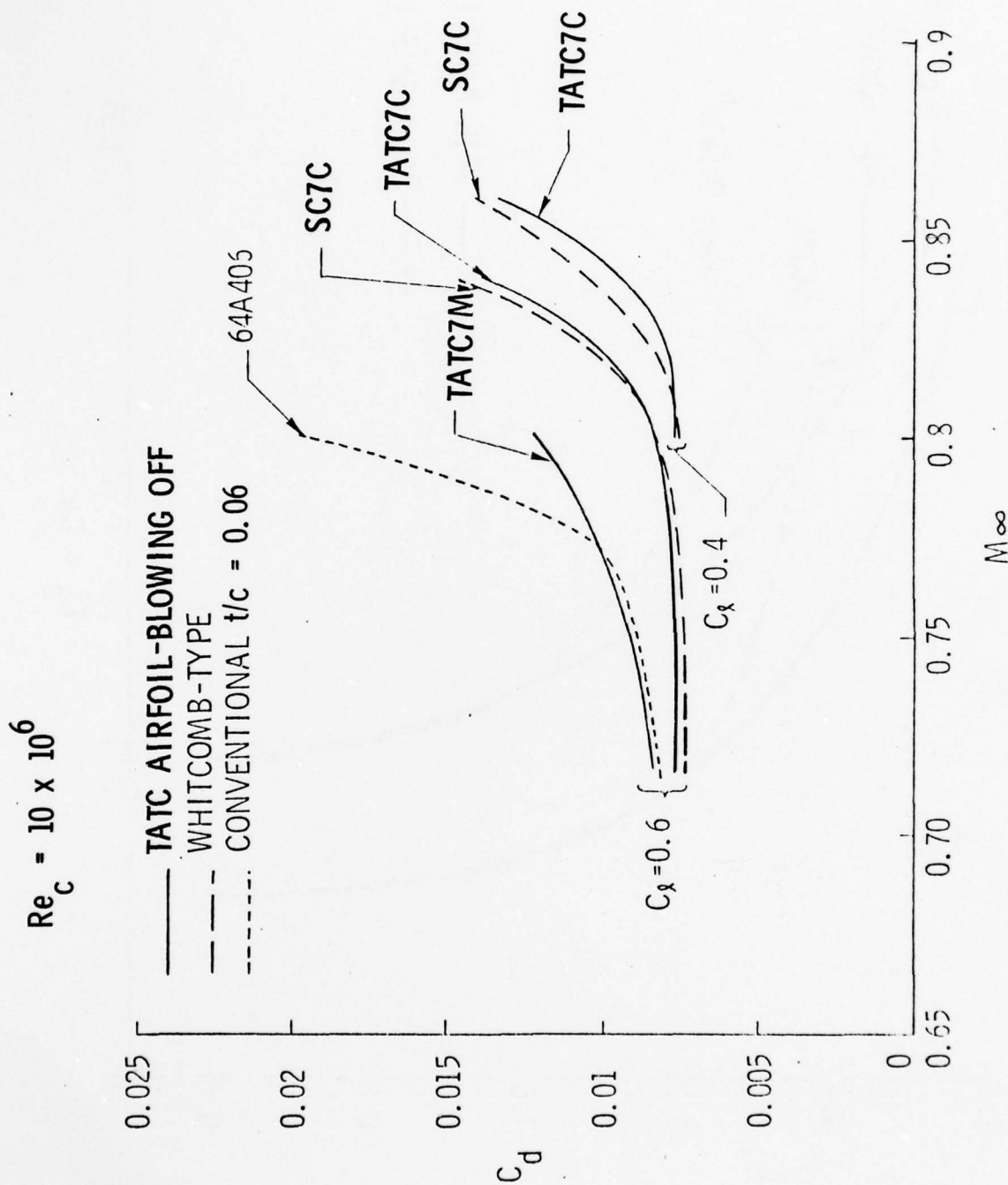


FIGURE 3-7 DESIGN PHASE COMPARISON OF DRAG DIVERGENCE

cruise baseline. Checks on pitching moment behavior were also made analytically and imply reduced trim penalties relative to the baselines except for the extreme lift/blowing conditions.

Since wind tunnel data follow in Section 5.0 and form the primary basis for study conclusions and recommendations, the above design results should be viewed as intermediate results that served to define the geometries and motivate the entry into model fabrication and wind tunnel testing tasks. To summarize the design results: maneuvering and cruise geometries with deployment commonality were determined for an advanced ATC airfoil with a seven percent thickness ratio; significant increments in maneuvering lift were predicted at equivalent drags relative to both Whitcomb-type and conventional airfoils; cruise deployment of the ATC airfoil at reduced blowing resulted in comparable design point performance and improved off-design characteristics relative to a Whitcomb-type baseline; and predicted maneuvering performance improvements carried through the full tunnel to flight Reynolds number range ($2.5-60 \times 10^6$).

3.3 PREDICTED BLEED POTENTIAL

A perspective on engine bleed requirements is presented in Figure 3-8 by comparing with the C_μ available from both by-pass and compressor bleed for a state-of-the-art P&W F401 engine installation. Because of the highly efficient ATC blowing, plenum pressure ratios in the 2-3 range are acceptable, thus making by-pass bleed a viable alternative to the more conventional compressor bleed arrangements. The C_μ required for the maneuvering design point (0.0128) is well within the capabilities of by-pass bleed while the C_μ required for the cruise design (0.0017) is attainable with compressor bleed. It should be noted also that the predictions for C_μ required are conservative, as previous experiments⁴ have verified, and the wind tunnel tests (Section 5.0) were oriented toward determining relaxed blowing requirements. Further, the C_μ predictions are for a chord Reynolds number of 10×10^6 and reductions will be obtained at Reynolds numbers approaching flight conditions. Bleed requirements are discussed again in Section 5.5 in terms of data results.

STATE-OF-THE ART ENGINE INSTALLATION

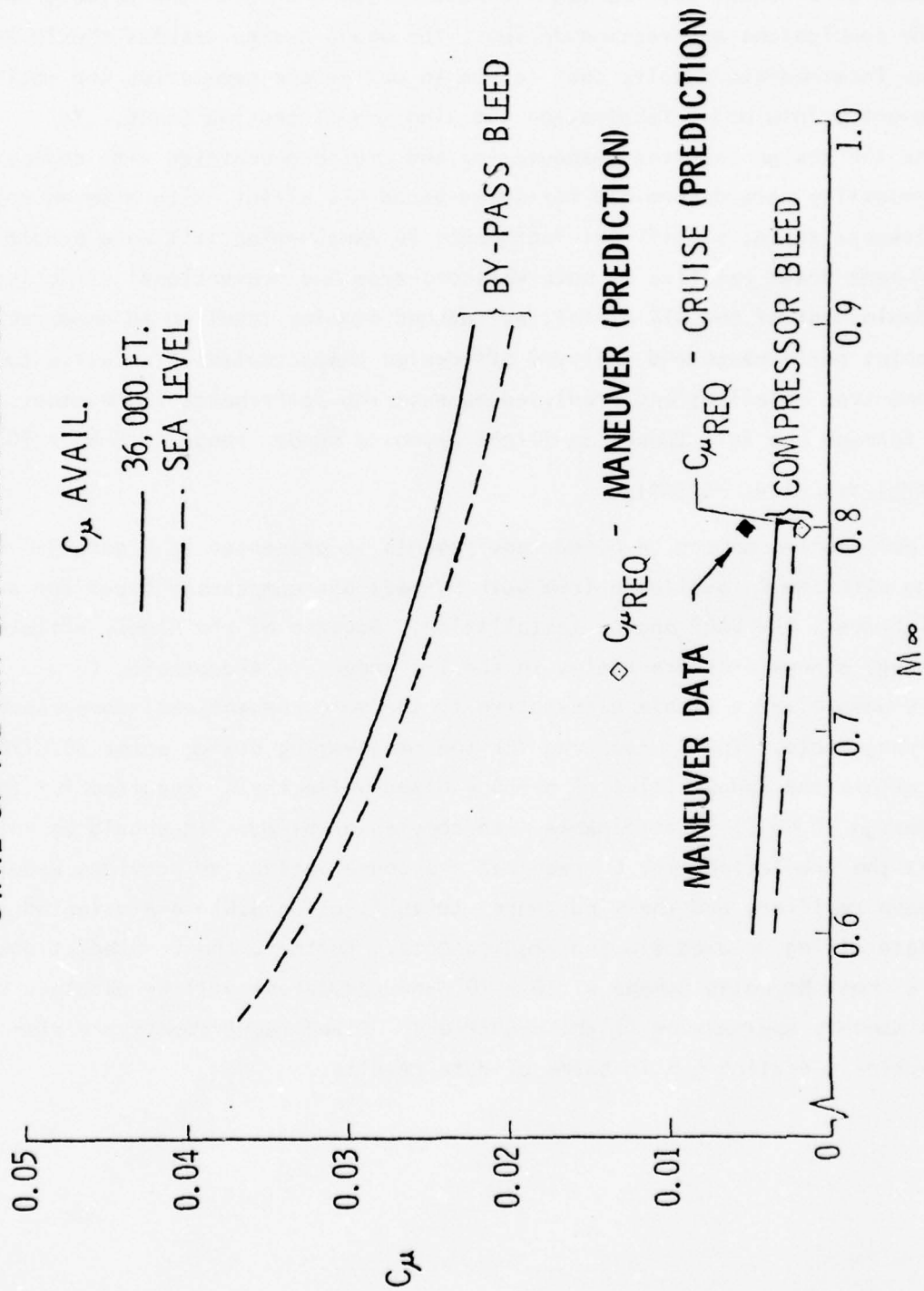


FIGURE 3-8 FULL SPAN BLOWING CHARACTERISTICS FOR A STATE-OF-THE-ART ENGINE INSTALLATION

4.0 HIGH SPEED WIND TUNNEL TESTS

4.1 FACILITY AND TEST ACCESSORIES

The transonic airfoil wind tunnel experiments were conducted in the High Speed Wind Tunnel (HSWT) facility of the Vought Corporation. The wind tunnel facility, model hardware, instrumentation, and data reduction are described in the following paragraphs.

4.1.1 High Speed Wind Tunnel

This is a variable pressure blow-down wind tunnel with a test section 1.22 m x 1.22 m (4' by 4') capable of Mach numbers from 0.5 to 5.0 and unit Reynolds numbers from 6 to 125 million per meter (2 to 38 million per foot). For the tests reported here the porous-wall transonic test section was used. All four walls have round holes perpendicular to the surface giving a total porosity of 22.5 percent. The holes are not adjustable but the porosity can be varied by covering a selected number of the holes with tape. In the tests of Reference 4, a wall interference-free porosity of seven percent was determined for an identical model/support arrangement. Strips of vinyl tape were placed length-wise along all four test section walls to attain this porosity. A sketch of the HSWT in the transonic configuration is shown in Figure 4-1.

4.1.2 Model Support System

An end-plated support assembly for the quasi-two dimensional testing of airfoil models was obtained on loan from the Propulsion Wind Tunnel Facility of Arnold Engineering Development Center, U. S. Air Force Systems Command. The assembly is shown in the sketch of Figure 4-2 and the photograph in Figure 4-3. It is the same hardware that was used at Vought in the blown airfoil tests of Reference 4. The sting-supported models were mounted on the tunnel model cart so that they could be pitched about a constant center of rotation on the test section centerline at test section station 67.

4.1.3 Instrumentation

Airfoil models were instrumented with static pressure taps which were connected via plastic tubing to modular pressure scanning switches (trade name, Scanivalve) mounted on the model cart sting support. Each modular unit contained a pressure transducer appropriate in range for the pressures measured and could measure up to 48 pressures per unit. All modules were synchronized to be sampled simultaneously at a rate of 5 samples per second.

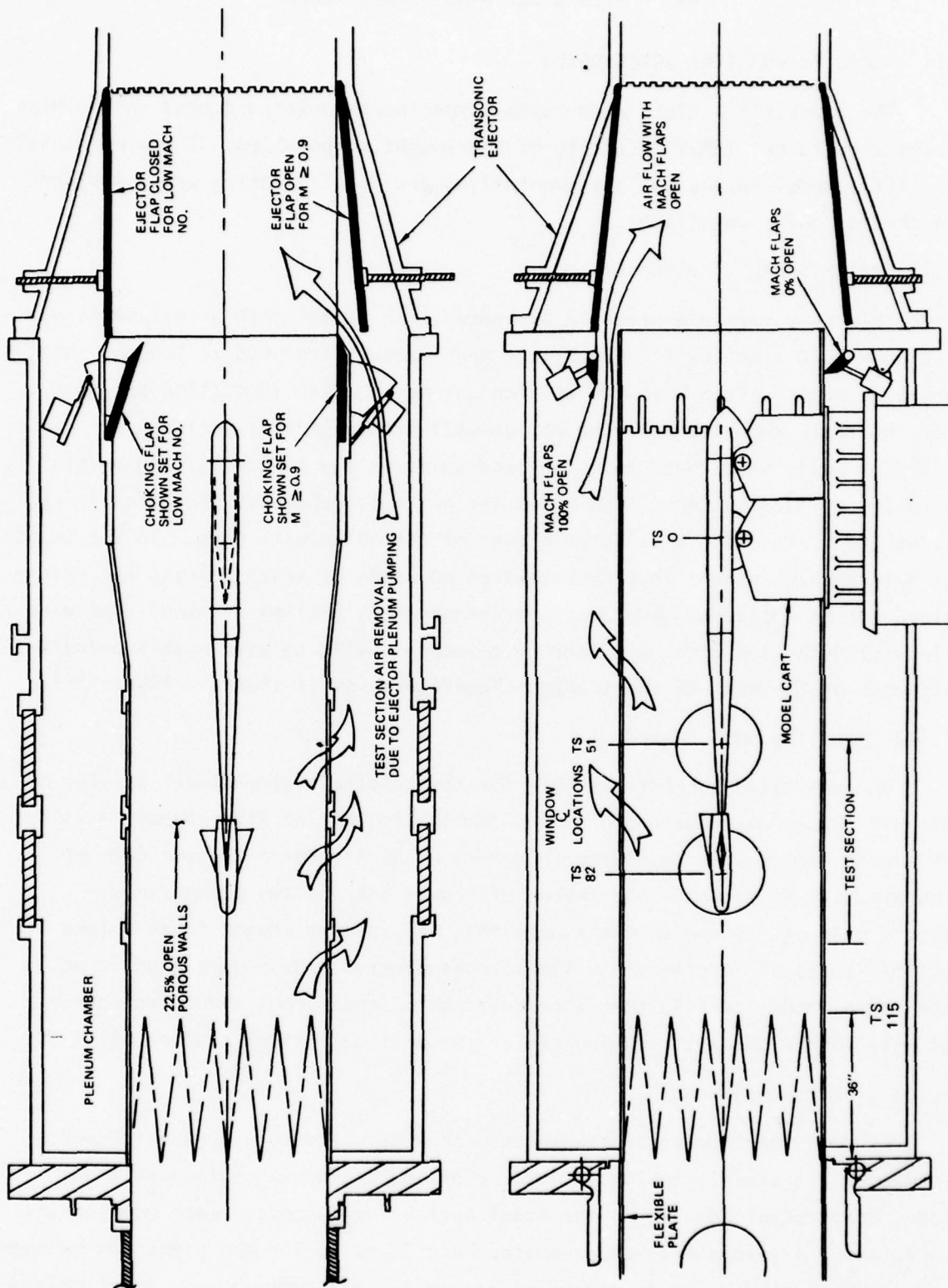
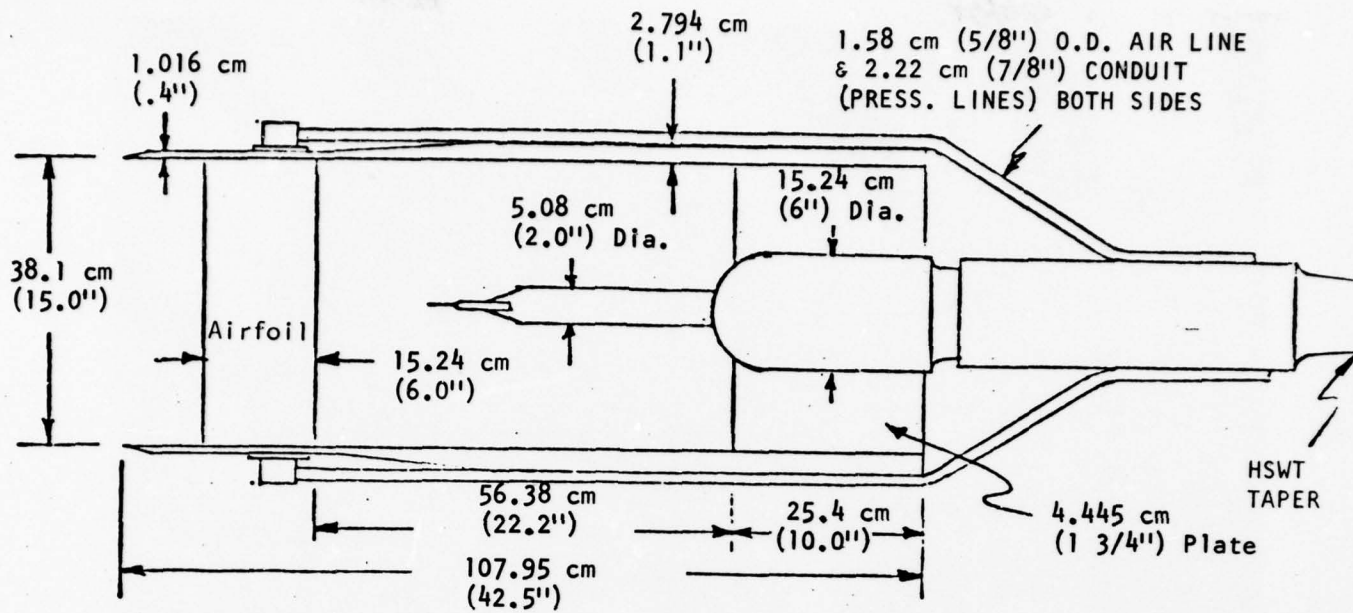


FIGURE 4-1 TRANSONIC TEST SECTION AND EJECTOR



1/10 SCALE (Approx.)

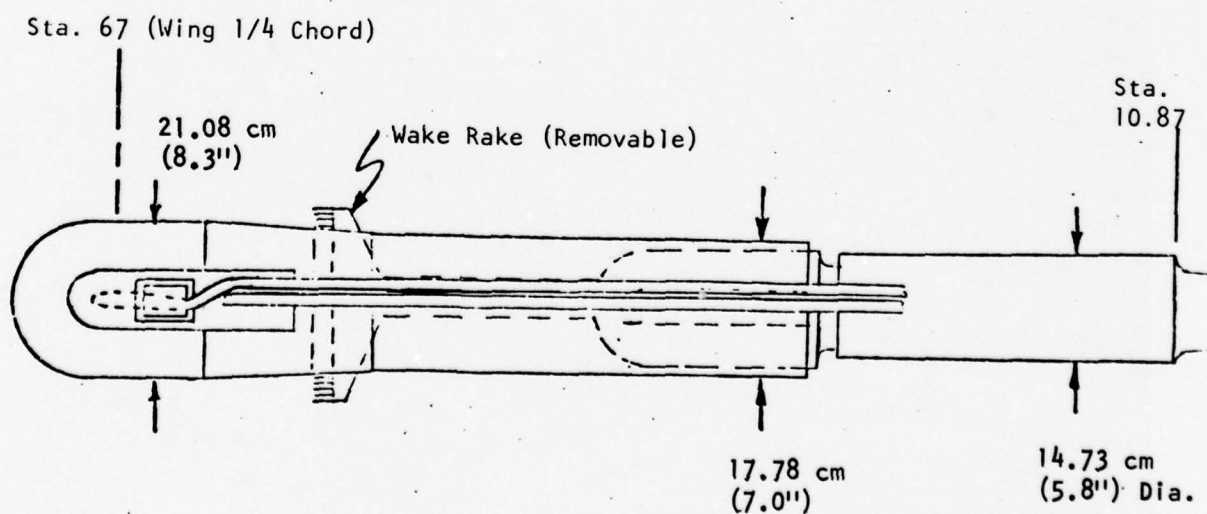


FIGURE 4-2 WIND TUNNEL TEST ASSEMBLY

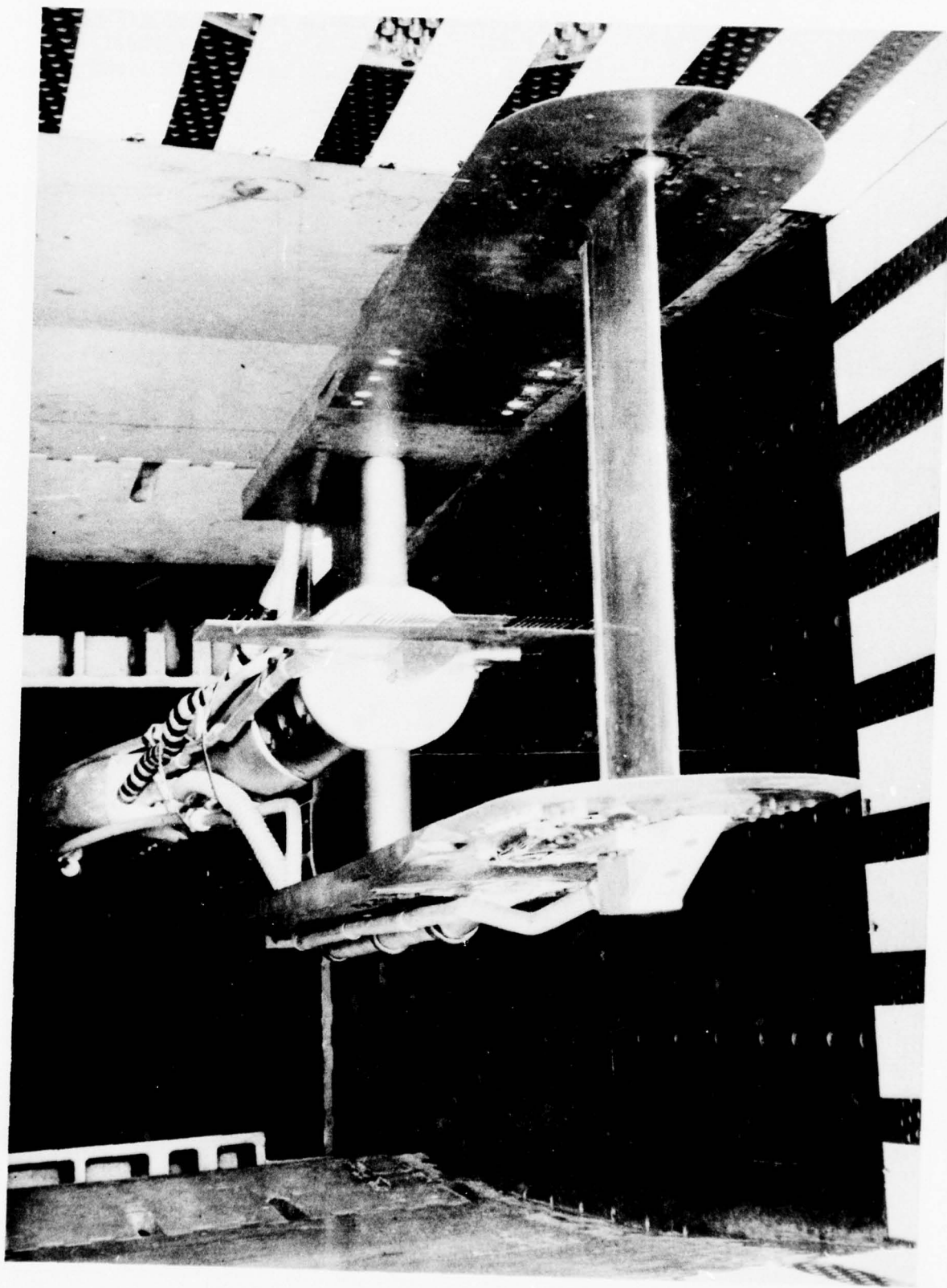


FIGURE 4-3 MODEL INSTALLED IN TUNNEL

A wake pressure rake with 61 total pressure probes and 3 static pressure probes spaced as shown in Figure 4-4 was mounted on the centerline of the model support apparatus at a distance of 2 model chord lengths behind the airfoil model trailing edge. The wake pressure rake along with the model taps were connected to a total of 3 Scanivalves.

For BLC blowing tests high pressure air was piped into the model support system from an auxiliary air supply in the HSWT facility. The auxiliary air was throttled to obtain desired pressure levels in the wing cavity. The air flow rate was measured with an orifice plate flow meter in the main supply line. The flow rate measurement, along with temperature and pressure measurements of the air in the wing cavity were used to calculate mass flow rate in the blowing jet. The temperature of the BLC air was measured with a chromel-alumel thermocouple mounted in the air fitting at one end of the blown wing. Two total pressure tubes were mounted in the wing cavity and monitored to set and maintain desired blowing pressures.

4.1.4 Data Reduction

Primary data reduction was accomplished immediately after each test run by an IBM 1802 computer on-line with the data system at the HSWT. Pressure data on the airfoil were reduced to coefficient form referenced to freestream static pressure and integrated to provide lift and pitching moment values. Data from the BLC blowing system were reduced and printed out in the form of blowing momentum coefficients (C_{μ}). The drag coefficient was obtained from integration of the wake total and static pressures which were used to define the wake momentum deficit. The equation used for the wake pressure integration has the form⁸

$$C_d = 2 \int_{\text{WAKE}} \left(\frac{P_{O_w}}{P_{O_\infty}} \frac{P_\infty}{P_w} \right)^{\frac{\gamma-1}{\gamma}} \frac{P_w}{P_\infty} \sqrt{\frac{1 - \left(\frac{P_w}{P_{O_w}} \right)^{\frac{\gamma-1}{\gamma}}}{1 - \left(\frac{P_\infty}{P_{O_\infty}} \right)^{\frac{\gamma-1}{\gamma}}}} \left[1 - \sqrt{\frac{1 - \left(\frac{P_\infty}{P_{O_\infty}} \right)^{\frac{\gamma-1}{\gamma}}}{1 - \left(\frac{P_w}{P_{O_w}} \right)^{\frac{\gamma-1}{\gamma}}}} \right] d\left(\frac{Z}{c}\right)$$

where

P_w = Static pressure at wake rake

P_∞ = Freestream static pressure

P_{O_w} = Total pressure registered by probe at wake rake

P_{O_∞} = Freestream total pressure

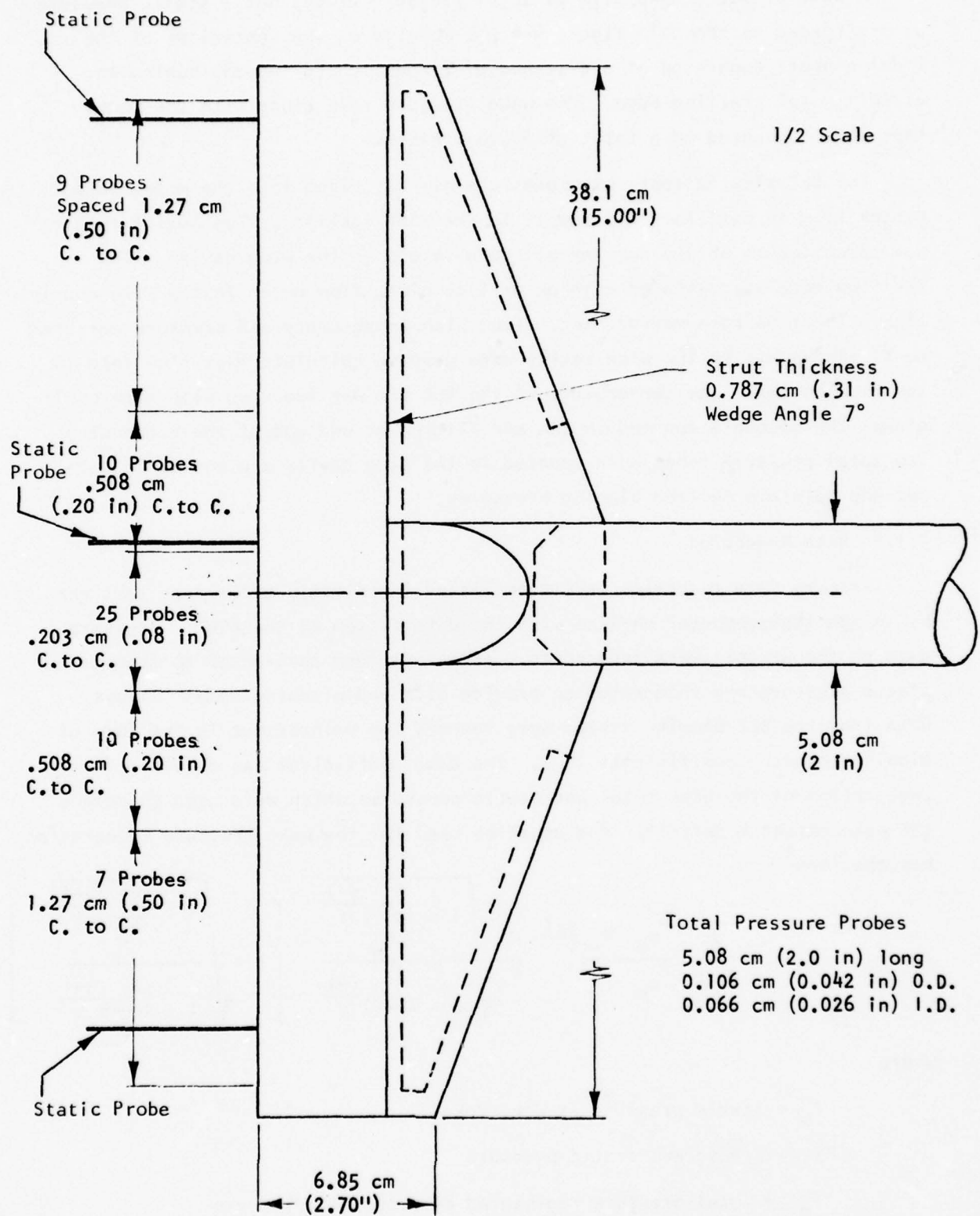


FIGURE 4-4 WAKE PRESSURE RAKE

4.2 DESCRIPTION OF MODELS

Model configurations were fabricated corresponding to both the maneuvering (TACT7M) and cruise (TACT7C) design points. Since the design points have deployment commonality, a common leading edge part and identical basic dimensions were used. The models have a chord of 15.24 cm (6 inches) and a span of 38.1 cm (15 inches) (Figure 4-2). They were constructed in two major segments; (1) a leading edge/upper surface (Part A), and (2) a lower surface/trailing edge (Part B). Sketches of the model parts and the associated assembly are shown in Figures 4-5 and 4-6. The leading edge/upper surface (Part A) provided a common attachment for the TACT7M maneuvering airfoil lower surface/trailing edge (Part B) and the TACT7C cruise airfoil counterpart. Surfaces of parts A & B form both the airfoil external contour and the internal access plenum/plenum webbing which feeds the blowing slot plenum.

The maximum thickness of 7 percent for both configurations is located at $x/c = 0.350$. The airfoil sections maintained a common airfoil shape forward of $x/c = 0.7$, differing only for slot adjustment and trailing edge camber aft of $x/c = 0.7$. The trailing edge designs provided both an antiseparation tailored contour and a two position deployment commonality. A nominal coordinate jump of $\Delta y/c = 0.0032$ at $x/c = 0.85$, is representative of the blowing slot gap of 0.0254 cm (0.010"), plus the thickness of the blowing lip edge of 0.0254 cm (0.010"). The percent chord size of the step in a full scale wing application would depend on lip tolerances and pressure ratio/slot gap trade-offs.

Both models were instrumented with 43 static pressures taps, Figure 4-7, located nominally at the center span of the models. The majority of the static pressure orifices have a 0.0508 cm (0.020 inch) diameter feeding into 0.1066 cm (0.042 inch) O.D. Monel tubing. At the trailing edge, the static pressure taps have an orifice diameter of 0.0228 cm (0.009 inch) and feed into 0.0508 cm (0.020 inch) O.D. Monel tubing coupled to the 0.1066 cm O.D. Monel tubing. The static pressure lines extend out both ends of the models and were connected via plastic tubing to the modular pressure scanning switches mounted on the model cart sting support.

The air supply for BLC was obtained from air lines routed along the side plates of the model support assembly and connected with sealed fittings to each

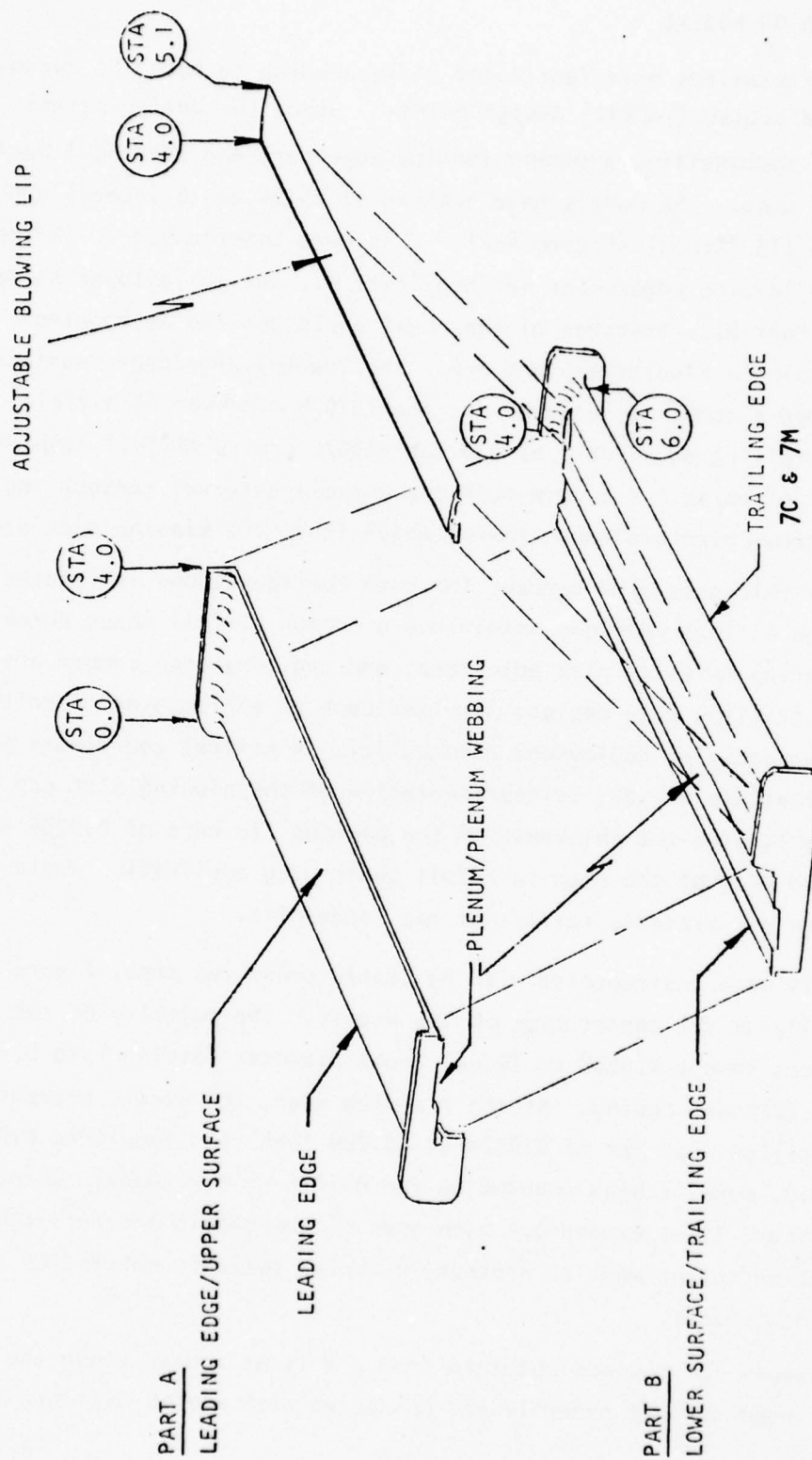


FIGURE 4-5 TATC7C, 7M WIND TUNNEL MODEL ASSEMBLY

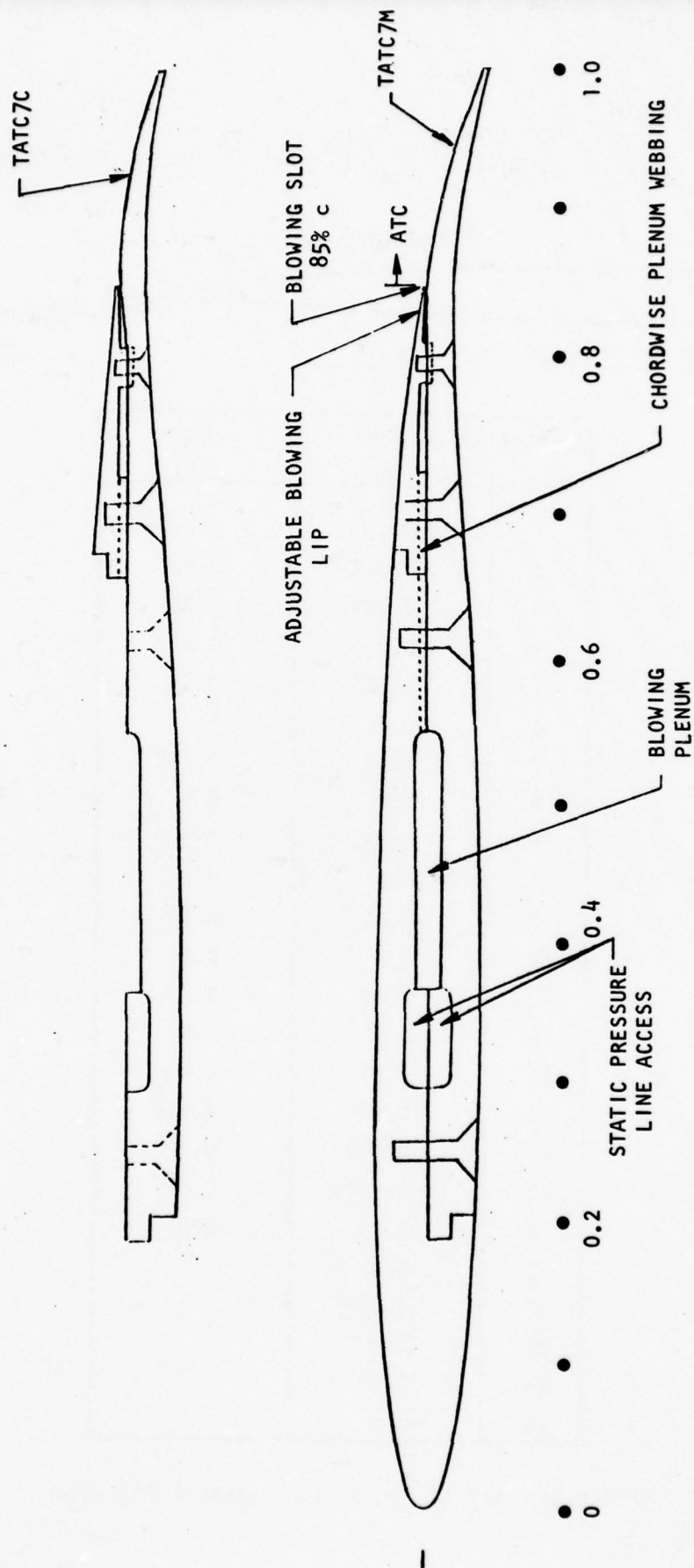
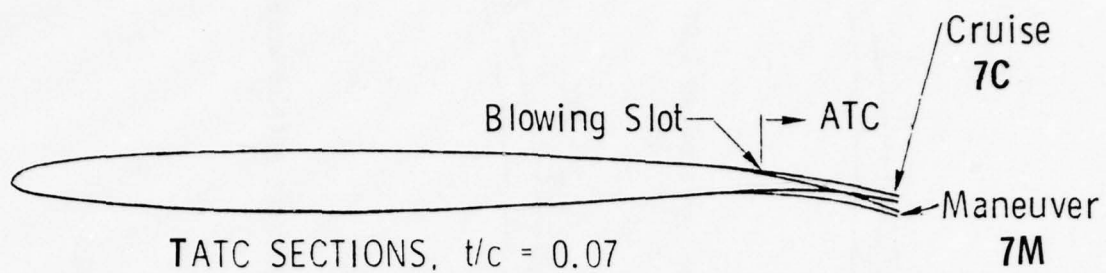


FIGURE 4-6 SCHEMATIC CROSS SECTIONS OF TATC7C, 7M HSWT MODELS



SURFACE:	UPPER X/C	LOWER X/C
1	0.0	0.0125
2	0.012	0.025
3	0.025	0.05
4	0.05	0.075
5	0.075	0.1
6	0.1	0.15
7	0.15	0.225
8	0.2	0.3
9	0.25	0.35
10	0.3	0.4
11	0.35	0.45
12	0.4	0.5
13	0.45	0.55
14	0.5	0.6
15	0.55	0.65
16	0.6	0.708
17	0.642	0.77
18	0.7083	0.84
19	0.75	0.93
20	0.8	
21	0.858	
22	0.9	
23	0.95	
24	1.0	

FIGURE 4-7 TATC7C, 7M STATIC PRESSURE ORIFICES

end of the model, Figure 4-2. These fittings were centered over the main access plenum cavity on each end of the model. The main access plenum cavity, shown in Figures 4-5,6, feeds the blowing slot plenum through an area of chordwise webbing used to increase the aft structural stiffness. Adjustments in the slot height are made with a row of screws located at $x/c = 0.795$. To insure uniform deflection of the adjustable blowing lip, a bending flexure was machined in the lip internal contour. A spanwise uniform slot height of 0.0254 cm (0.010 inches) was used throughout the testing.

4.3 TUNNEL CALIBRATION

The transonic airfoil test capability of the Vought High Speed Wind Tunnel was established in Reference 4 for quasi two-dimensional testing with the same sting/sidewall support hardware described above. Wall interference and porosity criteria were determined within the constraint of a nominal chord dimension of 15.24 cm (6 inches) and a related sting/sidewall sizing. Calibration data⁴ from unblown C-141 and blown ATC airfoil model tests provide a reference for the present testing. In these calibrations, the reliability and consistency of airfoil data obtained in the Vought HSWT at $Re_c = 2.5 - 6 \times 10^6$ were validated with respect to other test facilities (e.g., those at AEDC). The blockage distribution of the TATC model/support system appears in Figure 4-8. For this type of blockage, and the calibrated wall interference effects at the selected test conditions, the porosity was set at 7 percent (Section 4.1.1). Also, from Reference 4, a wake rake located at the present downstream distance of two chord lengths (Section 4.1.3) was found to have a negligible interference effect. Finally, although artificial boundary layer tripping was not used in the Reference 4 tests for a twelve percent thick blown section, it was added to the thinner TATC7M, 7C models to assist transition. A 0.0254 cm (0.1 inch) wide strip of #80 grit was used 1.27 cm (0.5 inches) aft of the leading edge.

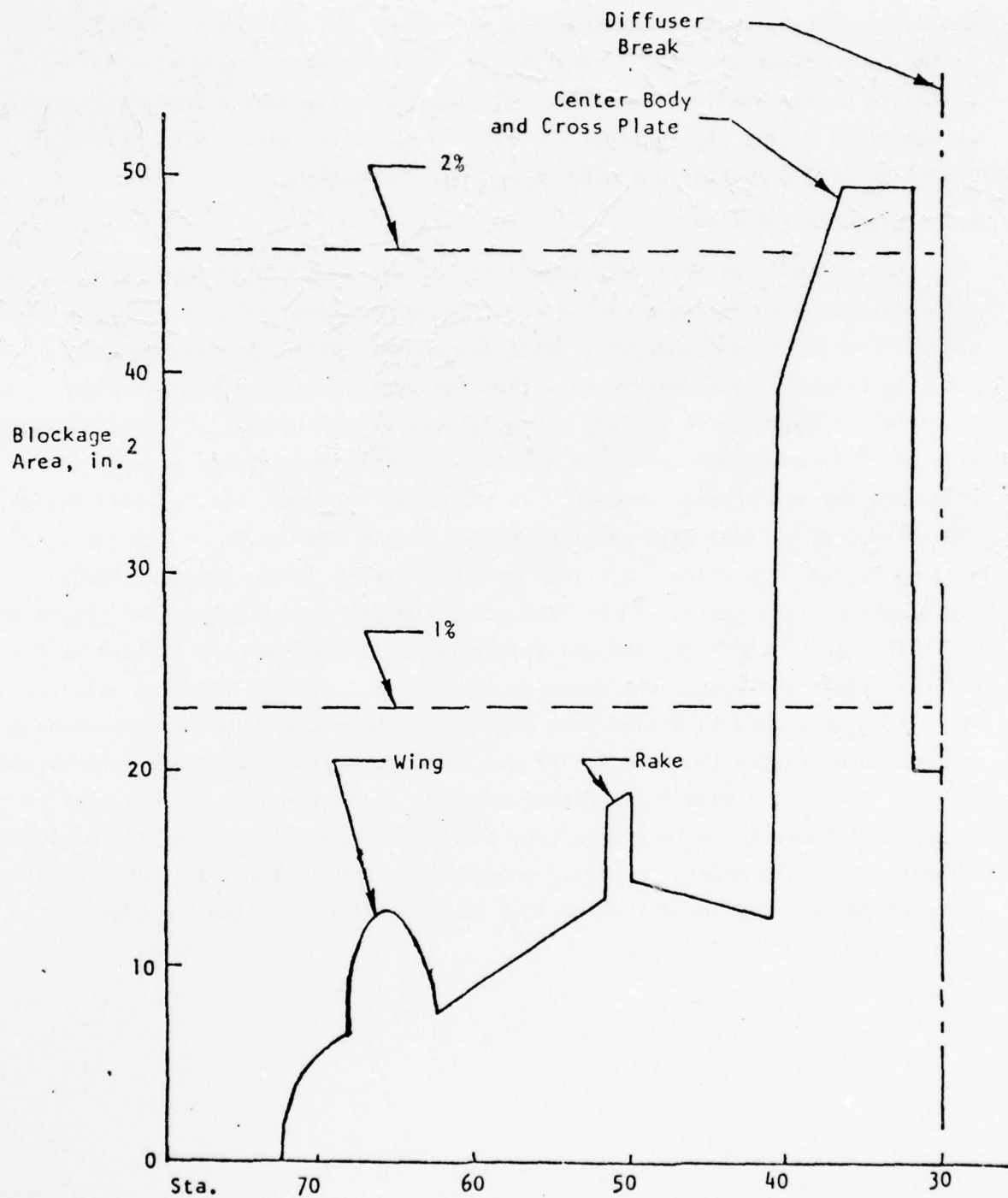


FIGURE 4-8 TEST SECTION BLOCKAGE OF TEST ASSEMBLY

5.0 TEST RESULTS AND DISCUSSION

5.1 RUN SUMMARY

Tests with the TATC airfoil models are summarized in Figure 5-1. The sequence of testing was to complete all tests with the TATC7M model first to determine maneuvering performance and then to install the TATC7C model and concentrate on cruise conditions. Runs with each model, however, covered both simulated cruise and maneuvering conditions to a sufficient degree to indicate off-design performance. Mach number/lift combinations for the TATC7C model were oriented toward determining drag divergence characteristics. Angles of attack varied up into regions of high wave drag and stall for both airfoils and jet momentum coefficients ranged from zero blowing to values exceeding the design predictions, even factoring in the Reynolds number effect in going from the $Re_c = 10 \times 10^6$ design to the 2.5×10^6 primary test condition. Test time constraints precluded extensive testing at the maximum tunnel Re_c of 6×10^6 but runs were made for selected cases to obtain an indication of scale effects. Airfoil pressure distributions, and lift (normal force C_N), drag, blowing, and quarter chord pitching moment characteristics are discussed in the following sections.

5.2 PRESSURE DISTRIBUTIONS

5.2.1 TATC7M Maneuvering Configuration

Initial tests revealed an anomaly between the ATC airfoil predictions and the data. Experimental pressure distributions are given in Figure 5-2 for $M_\infty = 0.73$, $C_\mu = 0.0178$ over a range of angle of attack that should encompass the roof-top TATC7M maneuvering design point of Figure 3-3. Instead, a "saddle" pressure distribution persists without development of a true roof-top. At low α the section is aft-loaded due to the trailing edge blowing/camber but, before the roof-top can fill in as α increases, leading edge shock separation appears. The design $C_\mu = 0.0128$ given in Figure 3-3 scales up to a level of 0.017 in going from design (10×10^6) to test (2.5×10^6) Reynolds numbers so blowing is close to the equivalent design level. As stated previously, the effective aft camber is a function of blowing (Section 2.1) and re-energization of the slot lip boundary layer perturbs the pressure distribution by reducing δ^* through the BLC region (Section 3.1). Detailing of the transonic mixing process through the assumed BLC control volume of Section 2.2 is a complex research task in itself. The predictive methods of Section 3.2, therefore, incorporate

MANEUVERING TATC7M					CRUISE TATC7C				
M	α°	NOMINAL C_μ	$Re_c \times 10^{-6}$		M	α°	NOMINAL C_μ	$Re_c \times 10^{-6}$	
0.73	0,3,4,7	0	2.4		0.80	-2,0,3,5	0	2.8-3.2	
	3,5	0	5.9				0.005		
	0,3,4,5,6,7,8	0.006	2.4-2.7				0.010		
		0.009-0.013					0		
0.80	0,3,5,7	0			0.84	0,3,5,7	0		
	5	0	6.1			-2,0,3,5	0.005		
	0,3,4,5,6,7,8	0.005-0.006	2.6-2.8			-2,0,3,5	0.010		
	0,4,6,8	0.007					0		
0.82	0,3,4,5,6,7,8	0.010-0.012			0.86	0,2	0		
		0.014-0.016					0.005		
	3,5	0.019				0,2,4	0.010		
						0,2,4	0.016		
0.83	0,2,4,6	0.011			0.90	4			
	-2,0,3,5	0.016					0.010		
0.83	-2,0,3,5	0.016			0.95	-2,0,2,4	0.010		

FIGURE 5-1 HSWT RUN SUMMARY

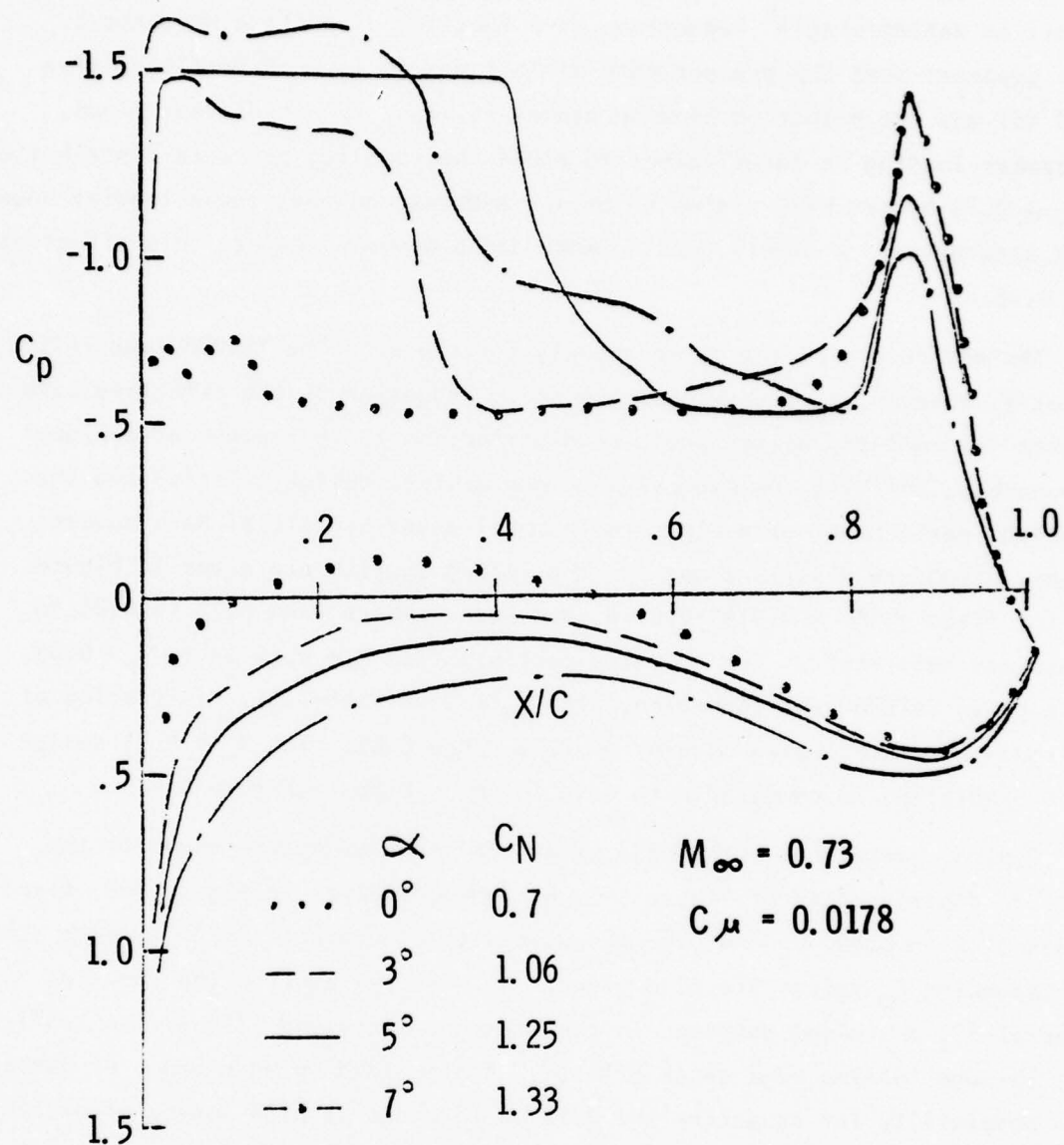


FIGURE 5-2 TATC7M PRESSURE DISTRIBUTION AT ANGLE OF ATTACK -
 $M_\infty = 0.73$, $C_\mu = 0.0178$

empiricisms successfully utilized in Reference 4 for a twelve percent thick airfoil in determining δ^* reductions as a function of surface distance S . It is apparent that the present thin airfoil design is much more sensitive to $\Delta\delta^*(S)$ and the effective blowing camber is less than predicted. Thus, aft camber loading is insufficient to close the roof-top pressure distribution at $M_\infty = 0.73$ before high angles of attack are reached that cause leading edge shock separation. A simple leading edge droop would alleviate this effect at $M_\infty = 0.73$.

The net result of the above anomaly for the existing TATC7M (and TATC7C) geometry, however, is a very positive one. Reduction of the effective camber permits the roof-top design pressure distribution to be reached at a higher Mach number, shifting the maneuvering (and cruise) design point(s) and the attendant performance gains to more innovative and beneficial Mach number ranges. Pressure distributions for the TATC7M section are given in Figure 5-3 for fixed α , $C_\mu = 0.0155$ - 0.0178 , and Mach numbers from 0.73 to 0.83 to illustrate this shift. The roof-top persists from $M_\infty = 0.80$ up to $M_\infty = 0.83$, the highest TATC7M test condition, with C_N 's from 1.06 - 1.15 . Initiation of the roof-top distribution occurs for $0.73 < M_\infty \leq 0.80$. The $M_\infty = 0.73$ design point prediction is compared with data for $M_\infty = 0.80$ in Figure 5-4.

Typical variations with angle of attack and blowing are shown in the pressure distributions of Figure 5-5, 6, respectively. In Figure 5-5, fixed values of $M_\infty = 0.80$, $C_\mu = 0.0161$ are used with α varying from 0° up into stall. Corresponding C_N values are also given. As α increases from the roof-top value of 3° , a minimum develops in the mid-chord area and lift is eventually lost through leading edge shock effects. Again, leading edge droop or camber is a possibility for enhancing the lift performance at high angles of attack in future ATC airfoil studies. Blowing is varied in Figure 5-6 from $C_\mu = 0$ up to 0.0161 for fixed $M_\infty = 0.8$, $\alpha = 3.0^\circ$. An increment of $\Delta C_N = +0.154$ is indicated over this blowing variation. As expected, the blowing-off distribution has no sharp aft upper surface diffusion step due to the onset of separation as indicated by the loss in trailing edge pressure recovery.

5.2.2 TATC7C Cruise Configuration

A Mach number shift in roof-top design pressure distribution was measured for the TATC7C model analogous to that described in Section 5.2.1 for the

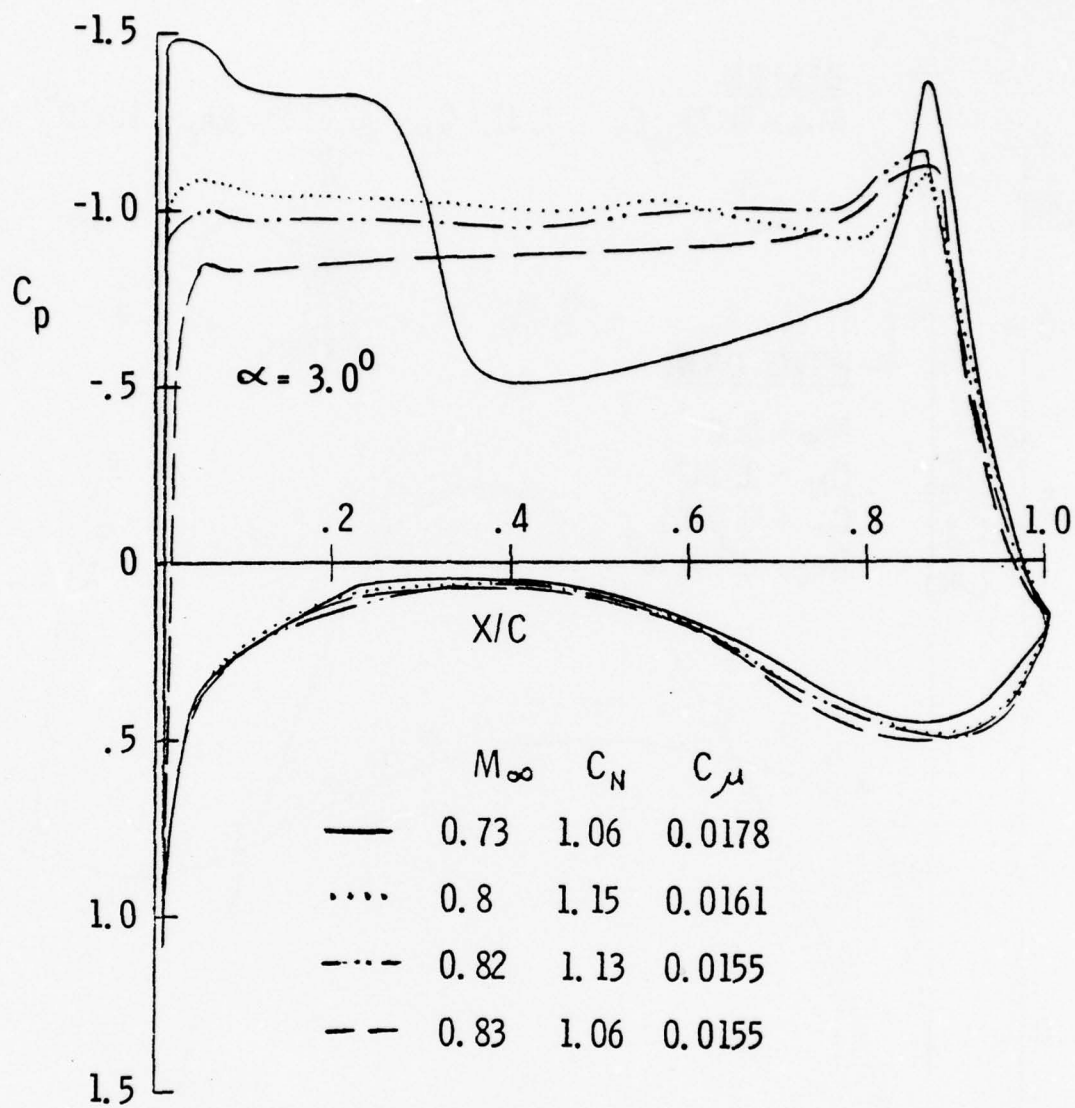


FIGURE 5-3 TATC7M PRESSURE DISTRIBUTION DATA AT MACH NUMBER - $\alpha = 3.0^\circ$

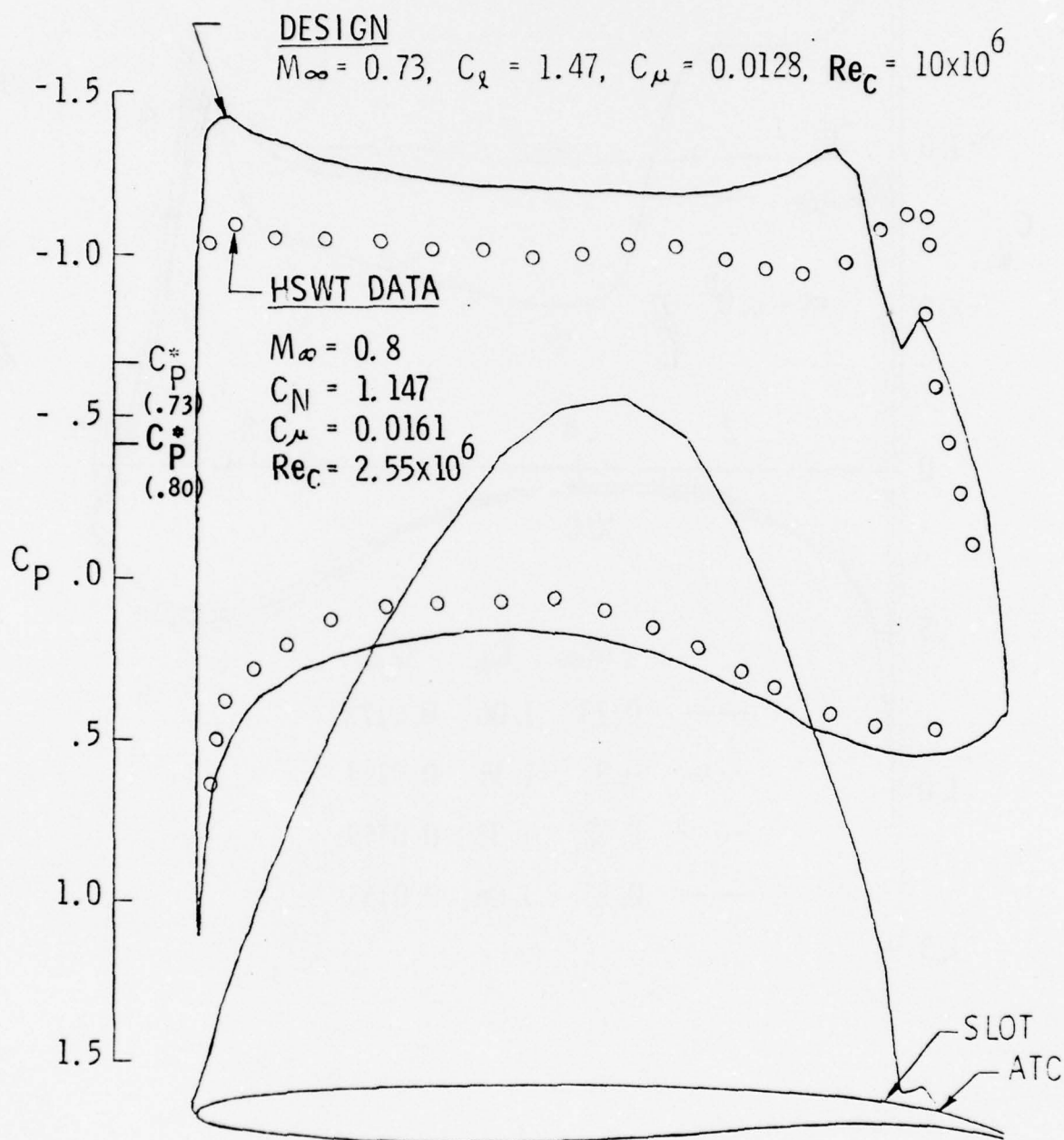


FIGURE 5-4 TATC7M MANEUVERING DESIGN POINT - DATA

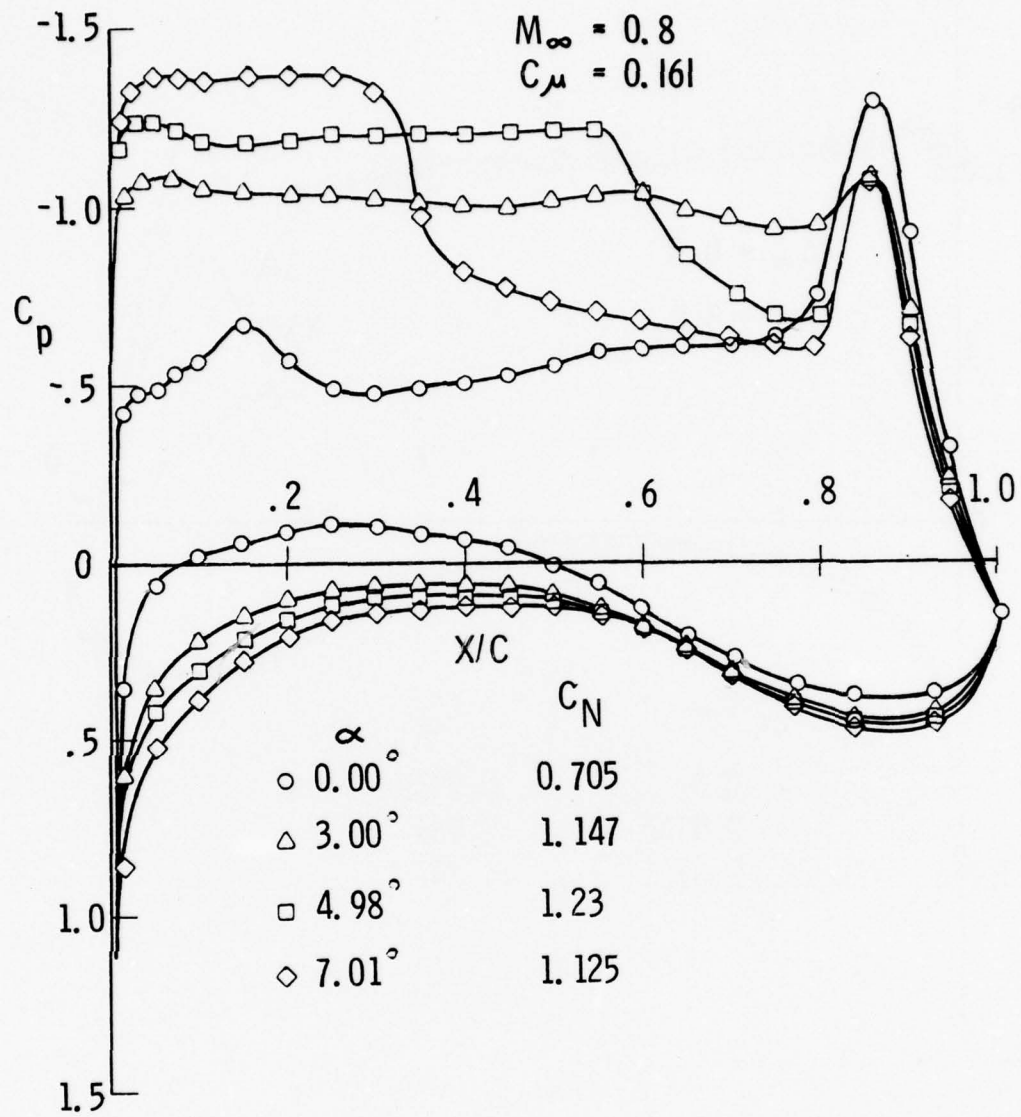


FIGURE 5-5 TATC7M PRESSURE DISTRIBUTION AT ANGLE OF ATTACK - $M_\infty = 0.8$, $C_\mu = 0.0161$

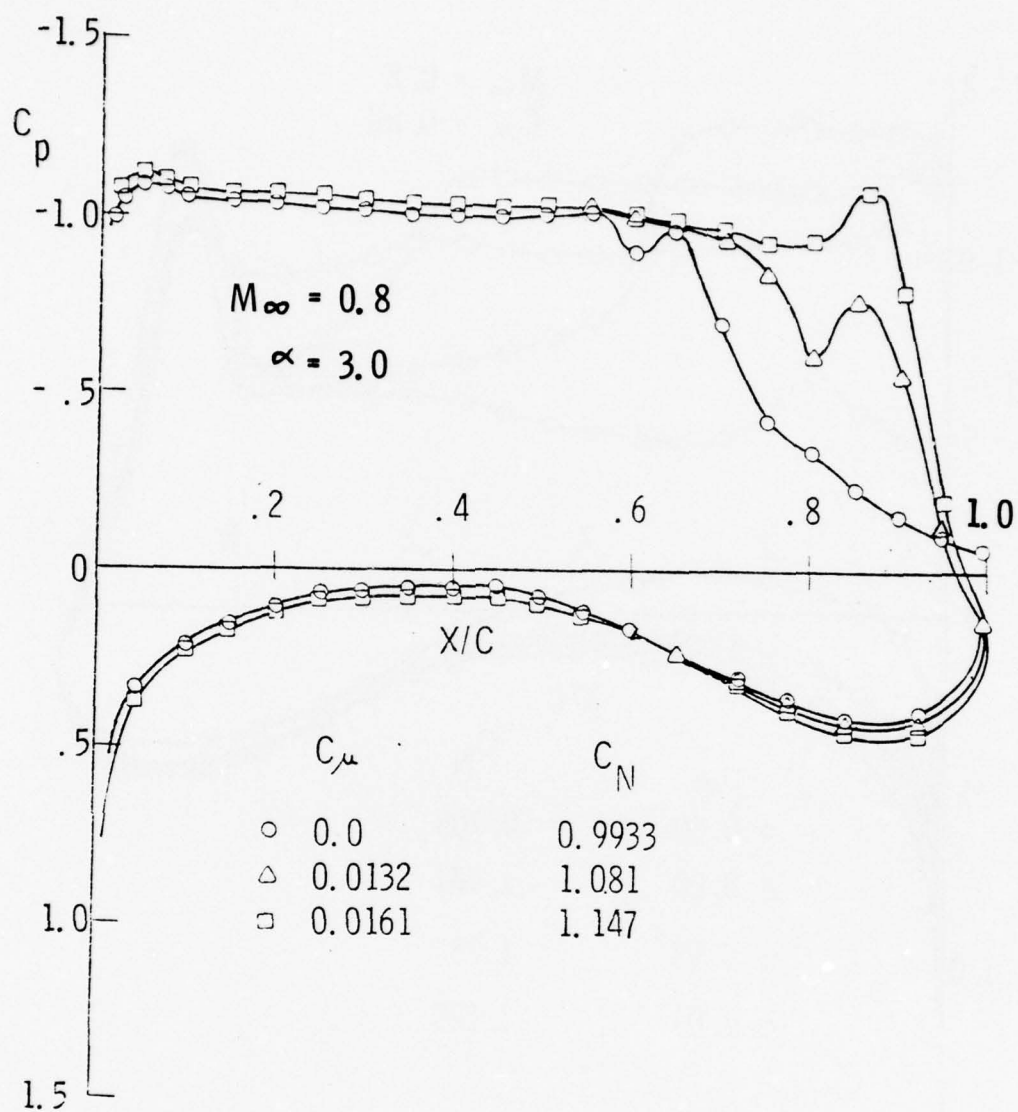


FIGURE 5-6 TATC7M PRESSURE DISTRIBUTION DATA AT BLOWING -
 $M_{\infty} = 0.8$, $\alpha = 3.0$

TATC7M configuration. Distributions for $M_\infty = 0.8, 0.84, 0.90$ are shown in Figure 5-7 at fixed $C_\mu = 0.005$ and nominal α in the 2-3 degree range. The $C_\mu = 0.005$ value is the closest blowing case to the design $C_\mu = 0.0017$ quoted in Figure 3-4. Approximate scaling of the predicted C_μ at $Re_c = 10 \times 10^6$ down to the $Re_c = 2.5 \times 10^6$ test conditions brings C_μ up to 0.0022. Even with overblowing, the plots in Figure 5-7 indicate aft loading for $M_\infty = 0.8, 0.84$ that departs considerably from the desired roof-top criteria. At $M_\infty = 0.9$, however, the criteria is achieved and the design point and the associated performance gains have shifted by $\Delta M_\infty = +0.1$.

The $M_\infty = 0.80, C_\ell = 0.6, C_\mu = 0.0017$ predicted design point distribution is compared with data at $M_\infty = 0.90, \alpha = 2^\circ$ in Figure 5-8. An interpolation between the $C_\mu = 0$ and 0.005 curves provides a good matchup with the aft upper surface shape of the prediction as well as the design $C_\ell = 0.60$. Leading edge pressures are almost identical for all cases while local Mach numbers are, of course, different due to the C_p^* shift. This figure also provides data at $M_\infty = 0.90, \alpha = 2^\circ$ that exhibits the effects of blowing variations. An increment of $\Delta C_N = +0.16$ is shown for C_μ changes from blowing off conditions up to $C_\mu = 0.010$. The blowing-off distribution has a reduced aft loading but shows no distinct separation or loss of pressure recovery at the trailing edge. This will be discussed further in Section 5.3.

Variations with angle of attack are shown in Figure 5-9 for the TATC7C section at $M_\infty = 0.9, C_\mu = 0.005$. In this limited range of $\alpha = 0, 2^\circ$, no unusual effects are encountered and the roof-top behavior generally exists for both plots. Scale effects are illustrated in Figure 5-10 for $M_\infty = 0.9, \alpha = 4^\circ$ and test Reynolds numbers of 3.0 and 6.0×10^6 . Alterations in the pressure distributions related to Re_c for this unstalled example are negligible. Only the very local spike at the blowing slot attributed to the significantly higher C_μ value for the $Re_c = 6.0 \times 10^6$ distribution is apparent.

5.3 LIFT/DRAG PERFORMANCE

Lift as a function of angle of attack is summarized in Figure 5-11 for representative TATC7M, 7C data. Comparisons are made with the ATC twelve percent airfoil (TEATC12) data of Reference 4 and data for a conventional C-141 section ($t/c = 0.12$) from Reference 9. The comparison data were taken with the same sting supported model hardware and thus provide the most direct C_N - α reference. Although the flow is quasi-two dimensional on the model,

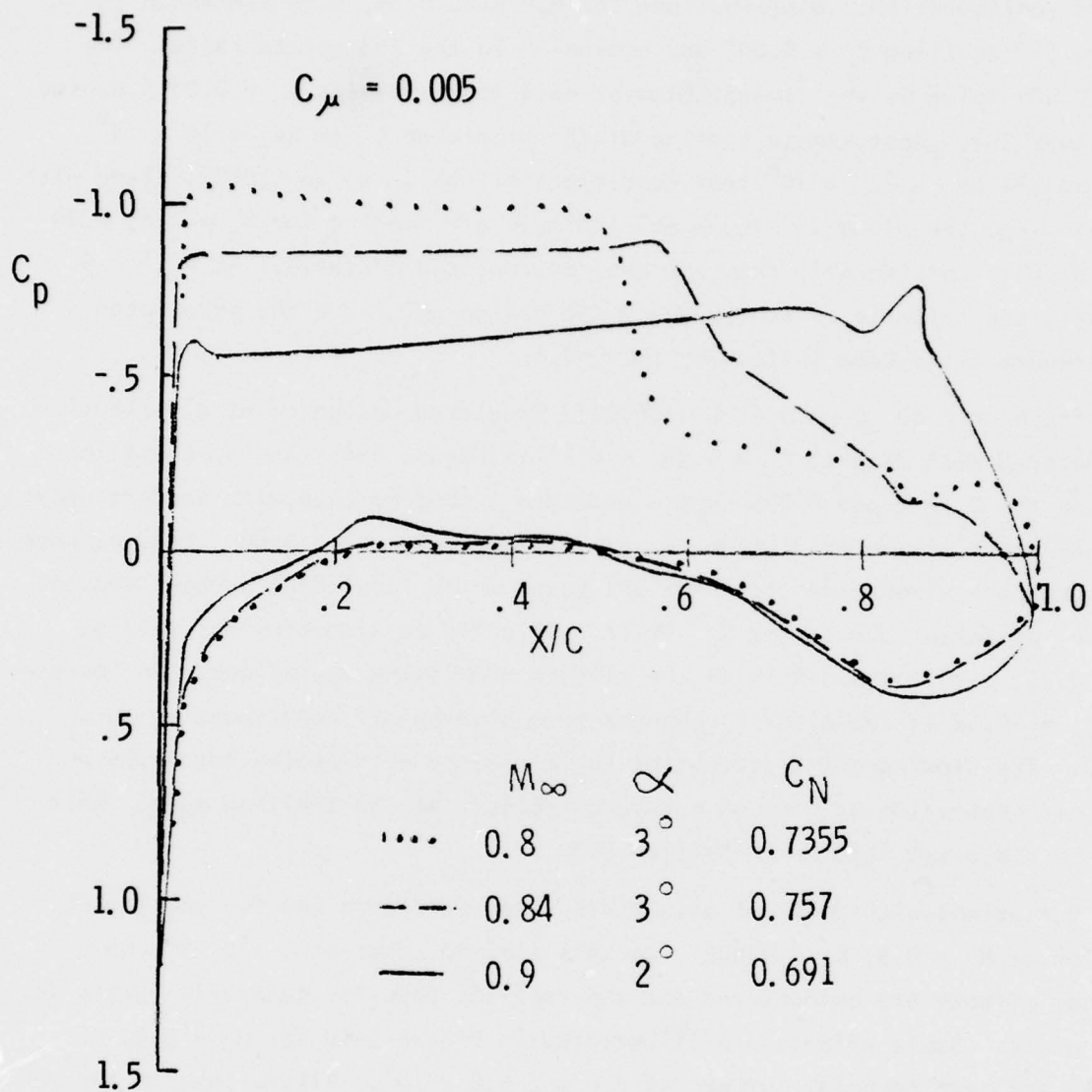


FIGURE 5-7 TATC7C PRESSURE DISTRIBUTION DATA AT MACH NUMBER - $C_{\mu} = 0.005$

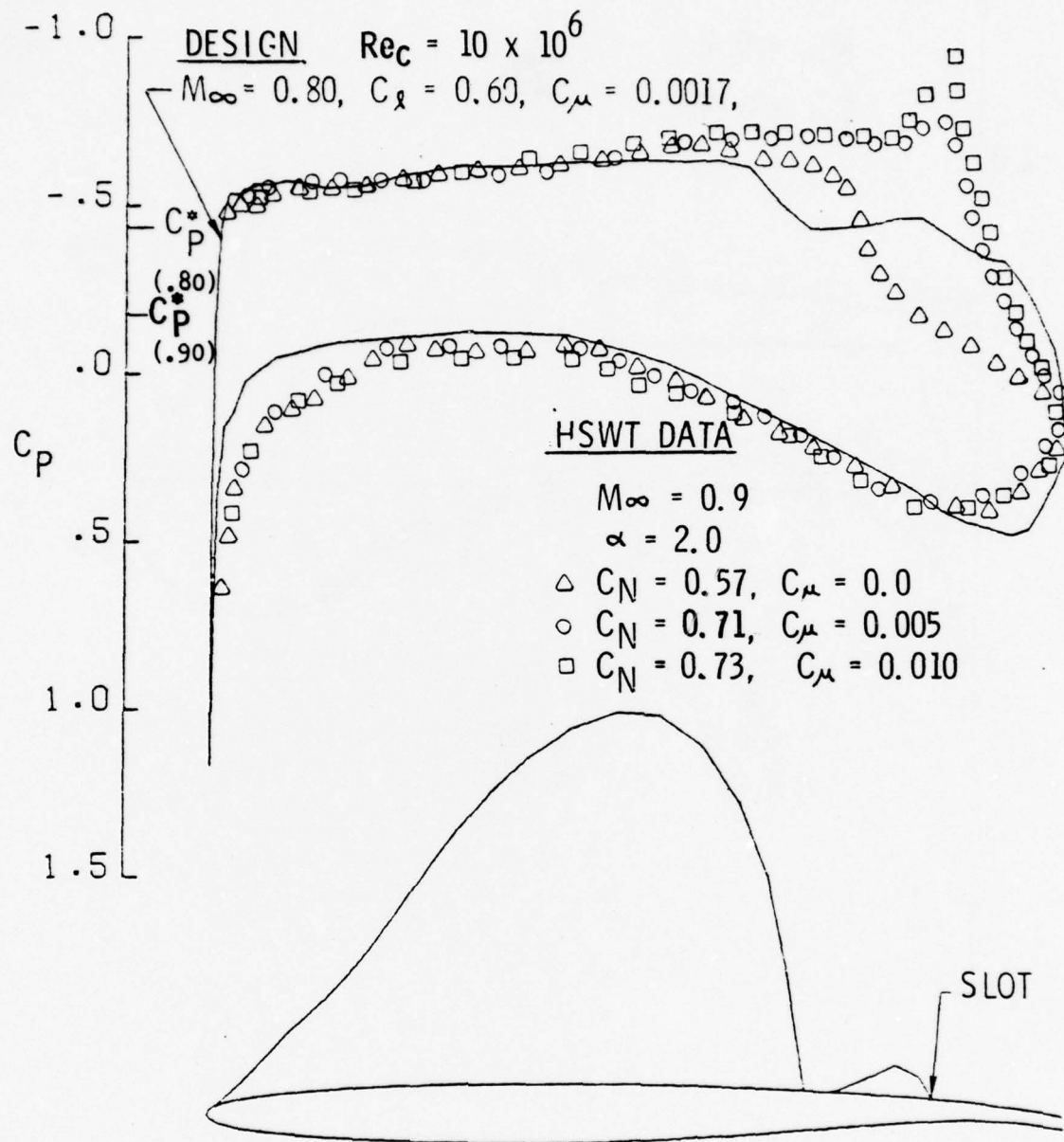


FIGURE 5-8 TATC7C CRUISE DESIGN POINT - DATA

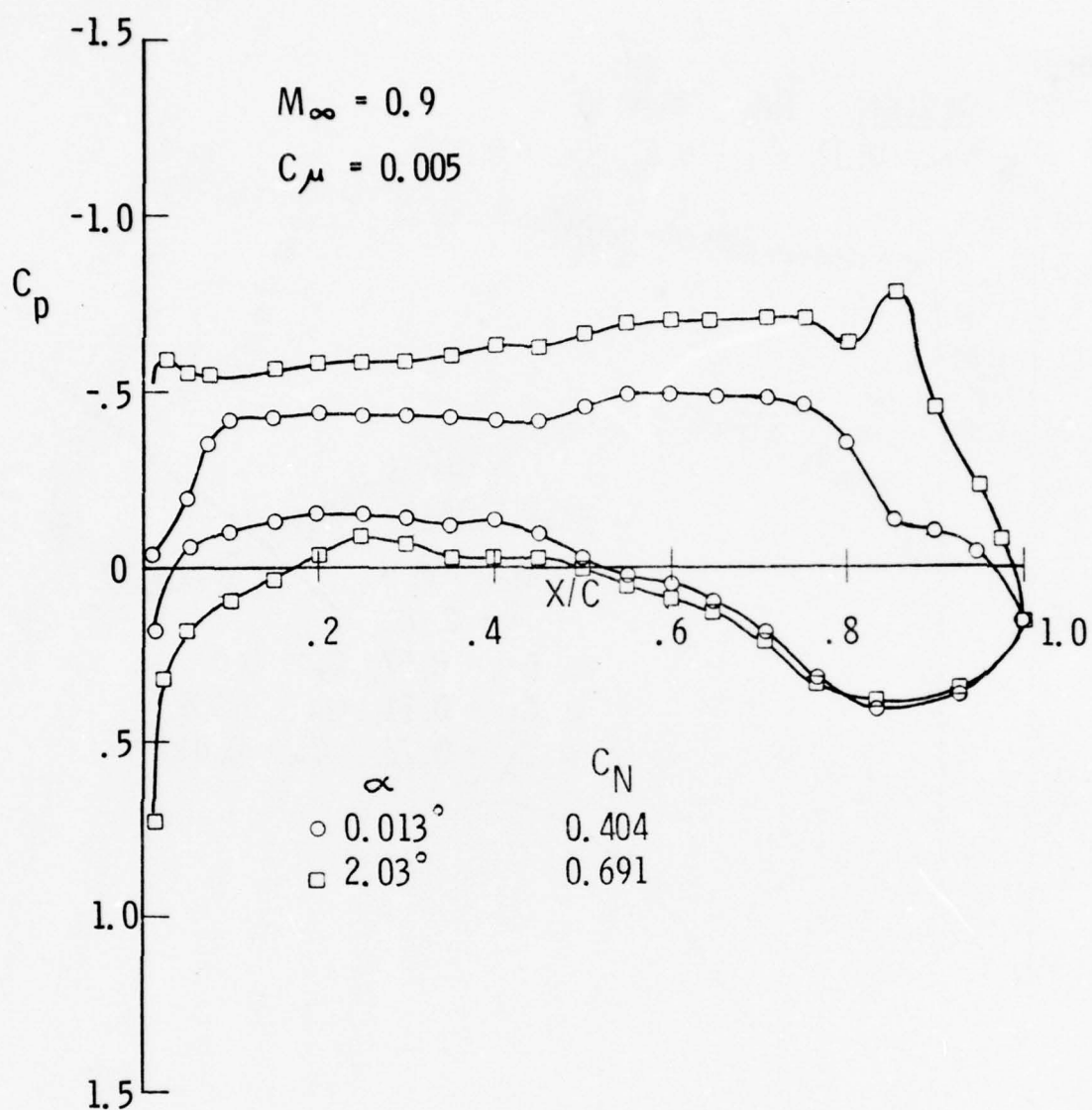


FIGURE 5-9 TATC7C PRESSURE DISTRIBUTION AT ANGLE OF ATTACK - $M_{\infty} = 0.9$, $C_{\mu} = 0.005$

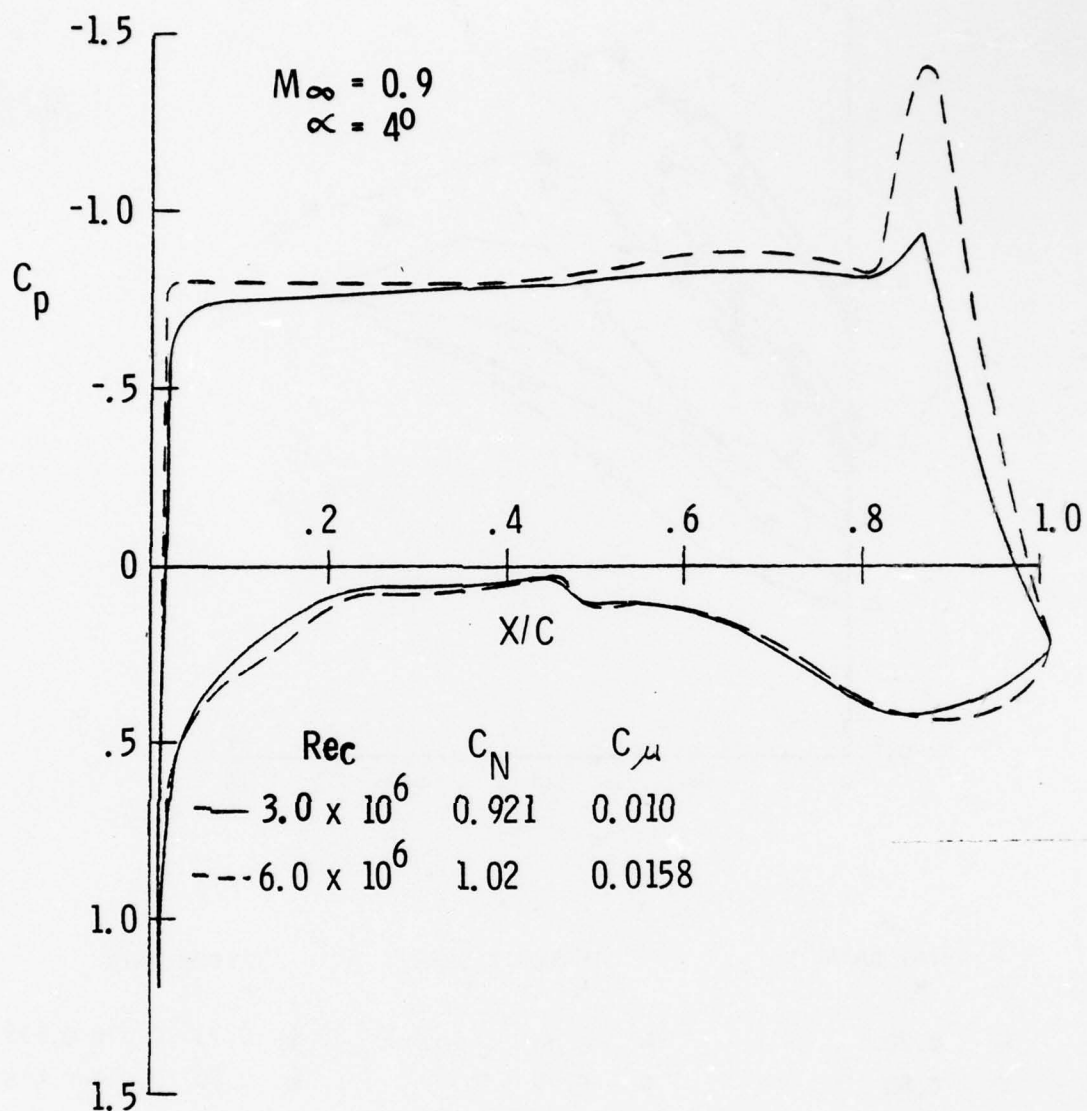
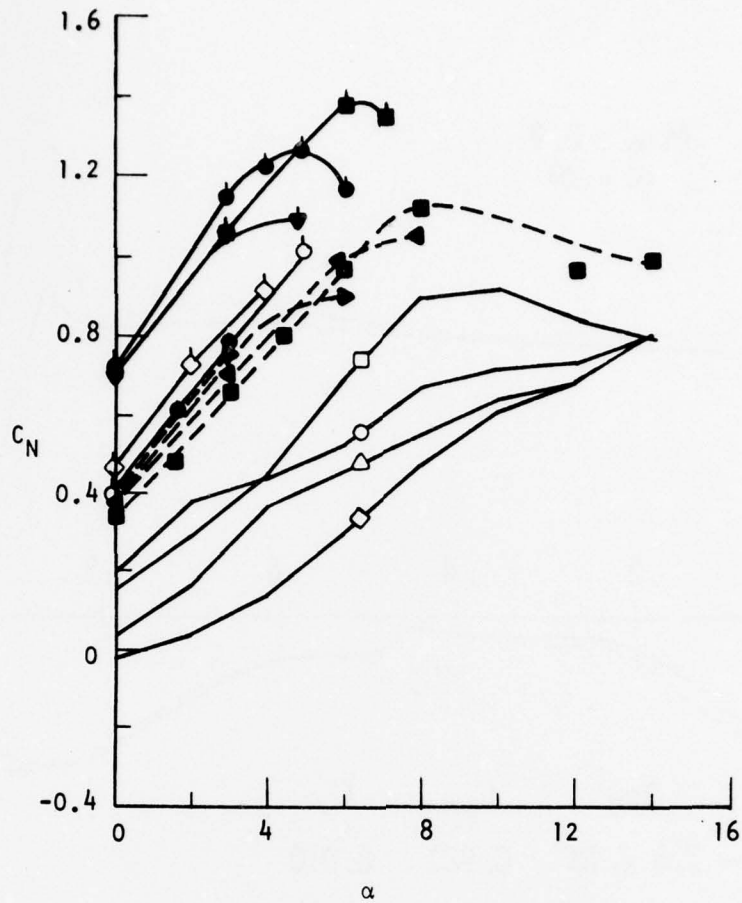


FIGURE 5-10 TATC7C PRESSURE DISTRIBUTION DATA AT REYNOLDS NUMBER -
 $M_\infty = 0.9, \alpha = 4^\circ$



C-141 DATA		TEATC 12 DATA		TATC7M DATA	
M_∞		M_∞	C_μ	M_∞	C_μ
□	0.70	■	0.70 0.0141	■	0.73 0.016-0.018
○	0.80	◐	0.75 0.0112	●	0.80 0.014-0.016
△	0.85	◑	0.77 0.0137	▼	0.82 0.016
◇	0.90	●	0.80 0.0133	TATC7C DATA	
				M_∞	C_μ
				○	0.80 0.010
				◇	0.90 0.010

FIGURE 5-11 TATC7M, 7C AIRFOIL LIFT CHARACTERISTICS

the support system provides a finite induced angle of attack which makes other C_N - α comparisons less valid. Increments on C_N at $\alpha = 6^\circ$ of +0.4 and +0.65 are shown for the TATC7M section, relative to the TEATC12 and C-141 twelve percent airfoils, respectively, in the $M_\infty = 0.70$ -0.73 range. At $M_\infty = 0.80$, $\alpha = 4^\circ$, the TATC7M C_N is 0.4 higher than that for the TEATC12 geometry. The TATC7C has a $C_{N_{MAX}}$ increment of +0.2 relative to the TEATC12 for $M_\infty = 0.80$ and $\alpha = 4$ -5°. Blowing coefficients for the TATC7 series are of the same order as those for the TEATC12.

As discussed in Section 2.2, $C_d + C_\mu$ is taken to be the equivalent section drag for the ATC airfoils. Plots of C_N vs. $C_d + C_\mu$ are given in Figures 5-12, 13 for $M_\infty = 0.8$, 0.9, respectively. The baseline Whitcomb-type SC7C, 7M airfoil performance (Section 3.2) has been re-calculated for $Re_c = 2.5 \times 10^6$ and analytical results are plotted in Figure 5-12. The SC7M high lift benefits shown in Figure 3-5 degrade significantly at low Reynolds number due to changes in displacement thickness creating higher drags and lower lifts. Experimental and analytical scaling effects need further investigation to improve the comparisons discussed below. Data for conventional 64A406, 64A006 sections are also utilized in Figure 5-12, 13.

Data is presented in Figure 5-12 for the TATC7M section at $M_\infty = 0.8$ with C_μ varying from 0 - 0.016. An additional plot for the TATC7C airfoil with blowing-off is included to emphasize lift advantages for the TATC7C to TATC7M deployment at $C_N > 0.6$ and to provide low drag data at $C_N < 0.6$. A performance envelope is shown representative of ATC variable geometry/blowing characteristics for the TATC7C, 7M combination. At equivalent drag, increments in maneuvering lift coefficient ($\sim C_N$) of +0.18 and +0.40 are measured relative to Whitcomb-type predictions and conventional airfoil data, respectively. These increments are comparable to the corresponding 0.18 and 0.50 values predicted in the ATC design phase at a lower Mach number of 0.73 (Section 3.2). Following the envelope to the lower C_N 's is indicative of continuous deployment from the maneuvering to cruise geometry and associated reduction in blowing toward blowing-off conditions. The drag levels at cruise $C_N < 0.6$ are less than or equal to those for the conventional section and approach the SC7C predictions. At zero blowing, the slot width becomes an aft facing step with a base drag contribution that ideally could be eliminated by slot closure, thus moving the TATC7C curve further to the left. It is interesting to note that, even with a slot drag contribution, the blowing-off TATC7M curve

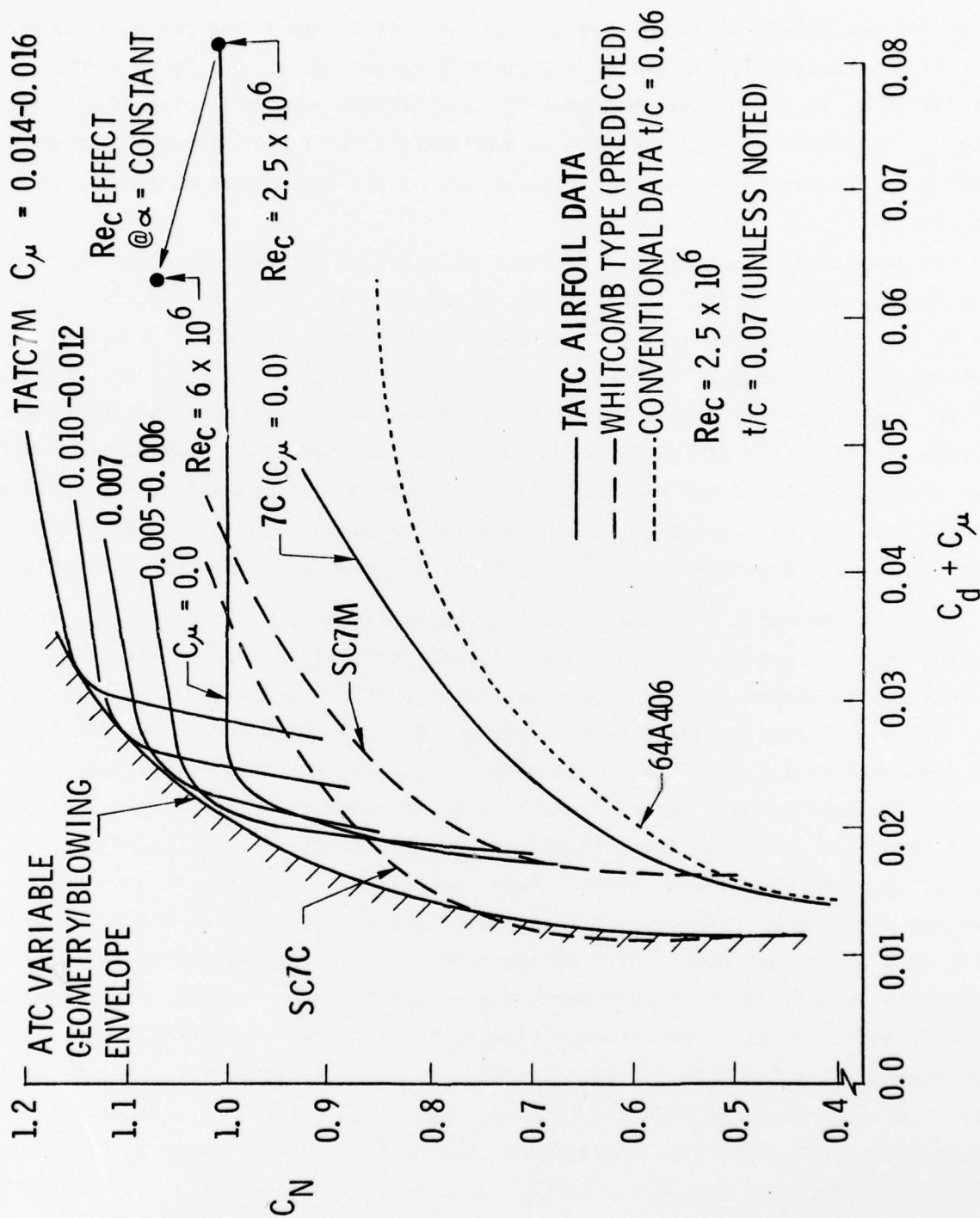


FIGURE 5-12 DRAG POLARS - $M_\infty = 0.8$

indicates improved C_N vs. C_d performance for $C_N = 0.86 - 1.0$ relative to the Whitcomb baseline. The separation illustrated in Figure 5-6 apparently reduces the effective upper surface curvature in such a way that decreased wave drag more than compensates for increased base drag.

Stall for the TATC7M airfoil in Figure 5-12 is very abrupt as a result of shock/boundary layer interactions at the low test $Re_c = 2.5 \times 10^6$. A data check was made in the stalled region at $Re_c = 6.1 \times 10^6$ for an angle of attack matching one of the $C_\mu = 0$, $Re_c = 2.4 \times 10^6$ points. An increase of 0.068 in C_N , accompanied by a decrease of 0.018 in C_d , was measured indicating a distinct softening of stall as Re_c increases.

Polars for the TATC7C configurations appear in Figure 5-13 for $M_\infty = 0.9$ and $C_\mu = 0, 0.005, 0.010$. Comparisons are limited to conventional 64A006, 64A406 sections since the analytical routines used for the Whitcomb-type baseline did not converge at $M_\infty = 0.90$ and no TATC7M data was acquired past $M_\infty = 0.83$. Zero blowing achieves the lowest equivalent drag at $M_\infty = 0.9$ and very low C_N but blowing-on is advantageous at cruise $C_N > 0.35$. In addition, the blowing-on curves show the ability to obtain ΔC_N increments of +0.12, relative to $C_\mu = 0$, for off-design cruise lift flexibility without deployment to the TATC7M geometry. Maximum measured C_N 's exceed 0.9. One key point in this figure is that, at $M_\infty = 0.9$, $C_\mu = 0.005$ performance is significantly better than that for either $C_\mu = 0$ or $C_\mu = 0.010$ on a C_N vs. $C_d + C_\mu$ basis. Because of the desirability of low blowing rates, the data base should be expanded to include C_μ between 0 and 0.005 for determination of a true blowing/performance optimum and a minimum C_μ -required.

Drag as a function of Mach number is plotted in Figures 5-14, 5-15, for the TATC7C airfoil at cruise $C_N = 0.4, 0.6$, respectively. Conventional and cruise SC7C curves appear for reference. The onset of drag divergence for the TATC7C is delayed by $\Delta M_{DD} = 0.08 - 0.09$ relative to the baseline Whitcomb calculations. Drag divergence Mach numbers (M_{DD}) of 0.92 are observed for blowing-on cases, indicating beneficial trades between C_μ , sized to skin friction losses, and the much higher losses associated with wave drag and separation. The pre-divergence TATC7C $C_d + C_\mu$ levels are higher than the C_d levels for the SC7C, although the $C_\mu = 0$ case for $C_N = 0.4$ (Figure 5-14) approaches equivalence. Blowing slot step drag contributes here to the levels for $C_\mu = 0$. Non-optimized blowing can also contribute to this effect since C_μ is

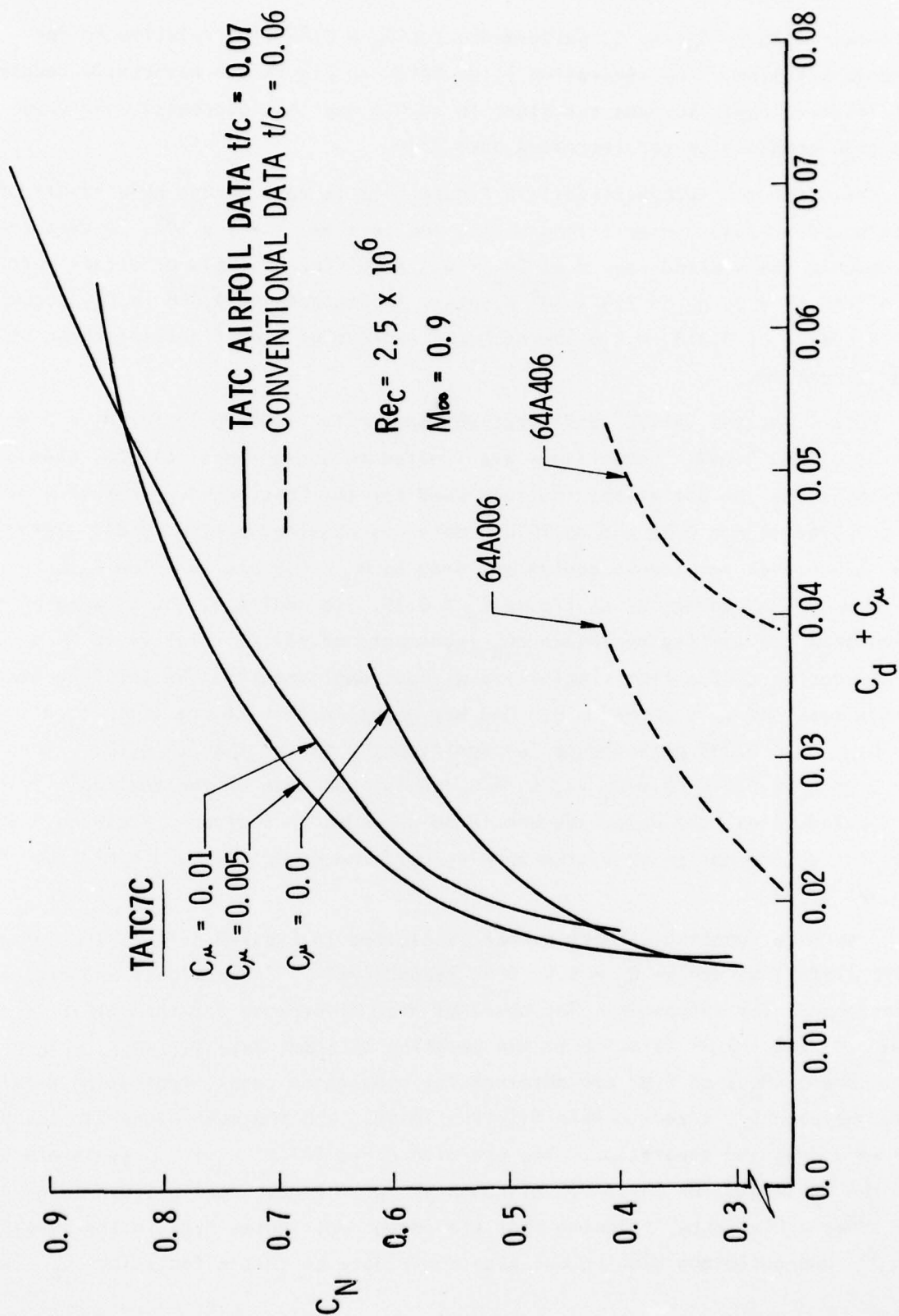


FIGURE 5-13 DRAG POLARS - $M_{\infty} = 0.9$

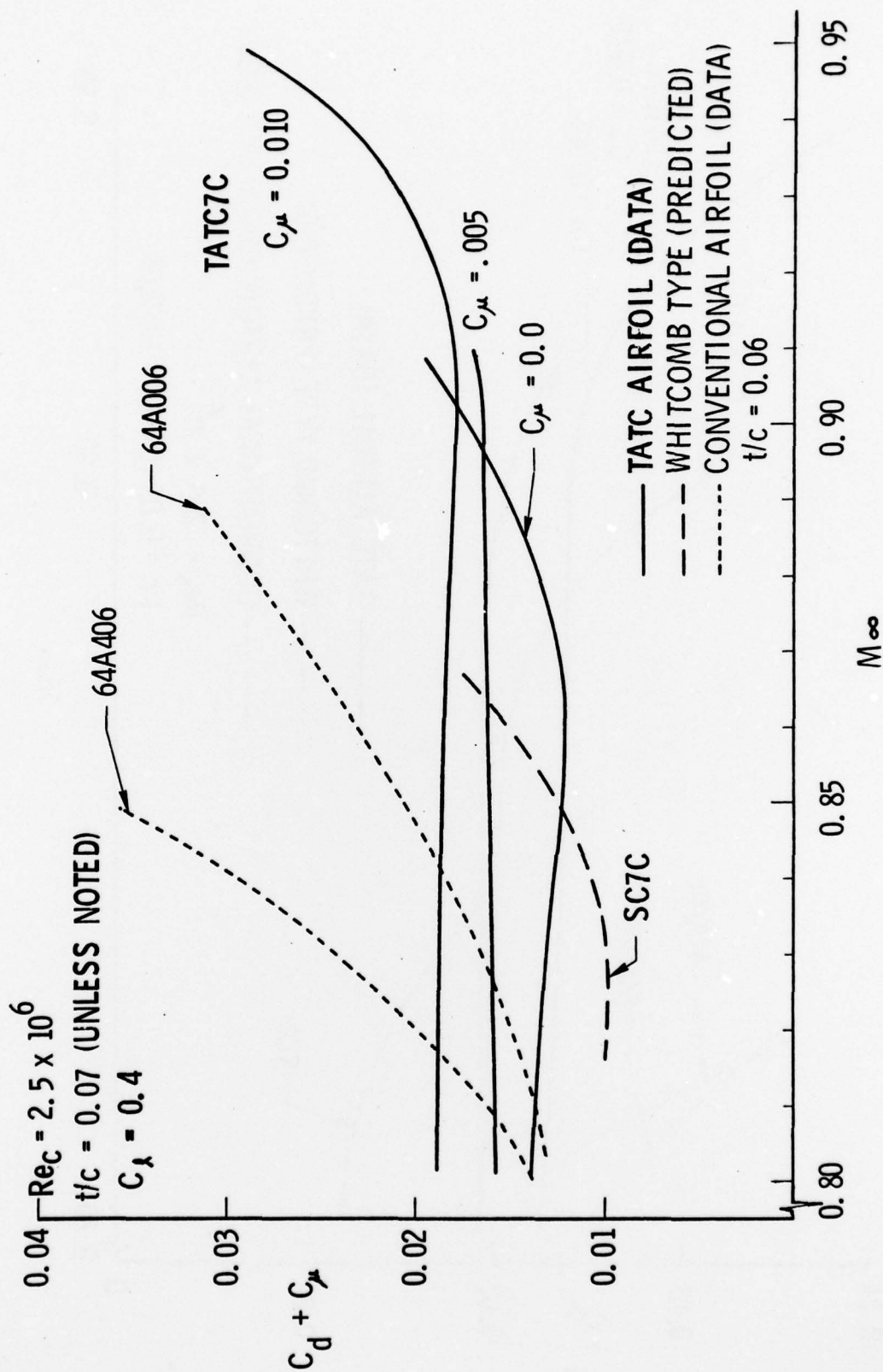


FIGURE 5-14 CRUISE DRAG DIVERGENCE - $C_\lambda = 0.4$

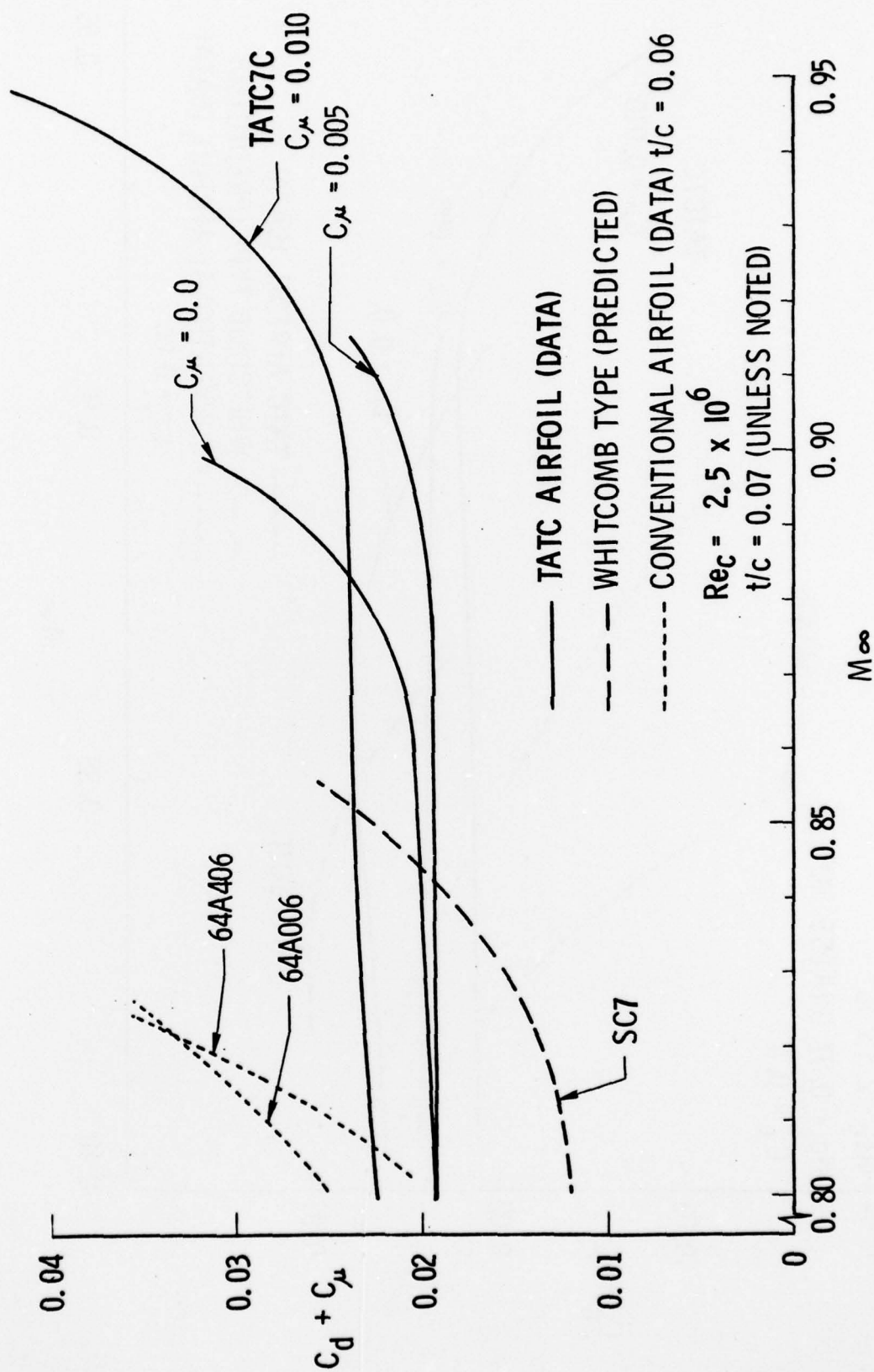


FIGURE 5-15 CRUISE DRAG DIVERGENCE - $C_\mu = 0.6$

25-50 percent of the total $C_d + C_{\mu}$. Performance at $C_{\mu} = 0.005$ exceeds that at either $C_{\mu} = 0$ or 0.010 for all plotted M_{∞} at $C_N = 0.6$ (Figure 5-15) illustrating the existence of a C_{μ} minimum and the relevance of future optimization. Tailoring of drag levels, at $C_N = 0.6$ for example, might be achieved through ATC deployments intermediate to the TATC7C and TATC7M geometries and refinements in the blowing rates as indicated by the envelope in Figure 5-12 for $M_{\infty} = 0.8$. The result of primary importance is that ATC blowing has the proven capability to alter the basic drag vs. Mach number behavior and delay drag divergence to M_{DD} values well over 0.9 .

Drag divergence comparisons, based on $C_d + C_{\mu}$, are made in Figure 5-16 as a function of airfoil thickness ratio for several airfoil sections, including the previous twelve percent ATC blowing geometry (TEATC12).⁴ Correlation curves are shown for both conventional and advanced supercritical designs at a cruise-type C_L of 0.5 . Calculated points for the SC7C baseline and for the TATC7C design point (Section 3.2) are also shown. The TATC7C prediction is conservative. The TATC7C data point exceeds the prediction by $\Delta M_{DD} = 0.08$ and falls above an extension of the supercritical correlation.

5.4 PITCHING MOMENTS

Pitching moments about the quarter chord point are plotted vs. C_N in Figure 5-17 for representative TATC7M, 7C data. Effects of Mach number and blowing are illustrated by varying M_{∞} from 0.73 to 0.80 and C_{μ} from 0 to 0.016 for the TATC7M airfoil and, correspondingly, utilizing $M_{\infty} = 0.80, 0.90$ and $C_{\mu} = 0, 0.010$ for the TATC7C section. Blowing effects on C_m for the maneuvering TATC7M geometry at both $M_{\infty} = 0.73, 0.80$ quantify the aft loading tendencies seen in the pressure distributions of Section 5.2. Pitching moments for the TATC7C are insensitive to blowing at $M_{\infty} = 0.8$ but reach the TATC7M sensitivity levels at $M_{\infty} = 0.9$. The high Mach number curves for both design points show monotonic increases in aft loading as α increases to stall. Overall, C_m variations for the complete range of ATC variable geometry/blowing configurations are limited to $|\Delta C_m| = 0.18$.

5.5 BLEED POTENTIAL - DATA

Section 3.3 discusses predicted C_{μ} -available/required matchups between the ATC airfoil and a state-of-the-art engine installation. The data plotted in Figure 5-12 provide additional indications of realistic bleed potential that

AIRFOIL SECTIONS				
SYM	SECTION	TYPE	$P_{eq} \times 10^{-5}$	REF
●	TATC7C	ATC	2.5	4
■	TEATC/12%	(DATA-FLAGGED)	2.9	7
○	64A406	Conventional (Data)	2	7
♀	64A006		2	7
□	64A410		2	7
♂	64A010		2	7
△	C-141		2.5	9
◇	Basic/10%	Non-Peaky	13-30	3
⋈	A/10%	Supercritical (Data)	13-30	3
○	K-2		6	10
⋈	K-2		10	10
▽	K-3		10	10
▽	Whitcomb Slotted		-	11
▽	Whitcomb Unslotted	"	-	12
⋈	SC7C	(Analysis)	2.5-10	

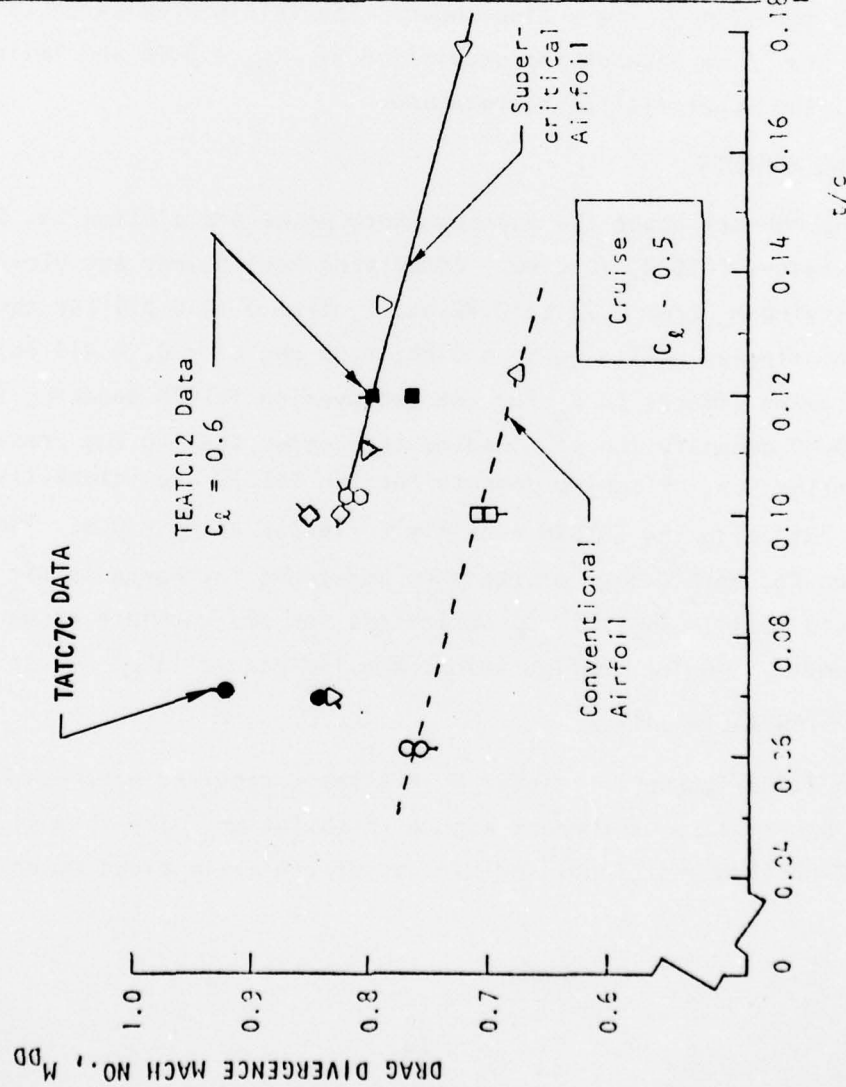


FIGURE 5-16 DRAG DIVERGENCE MACH NUMBER vs. THICKNESS RATIO

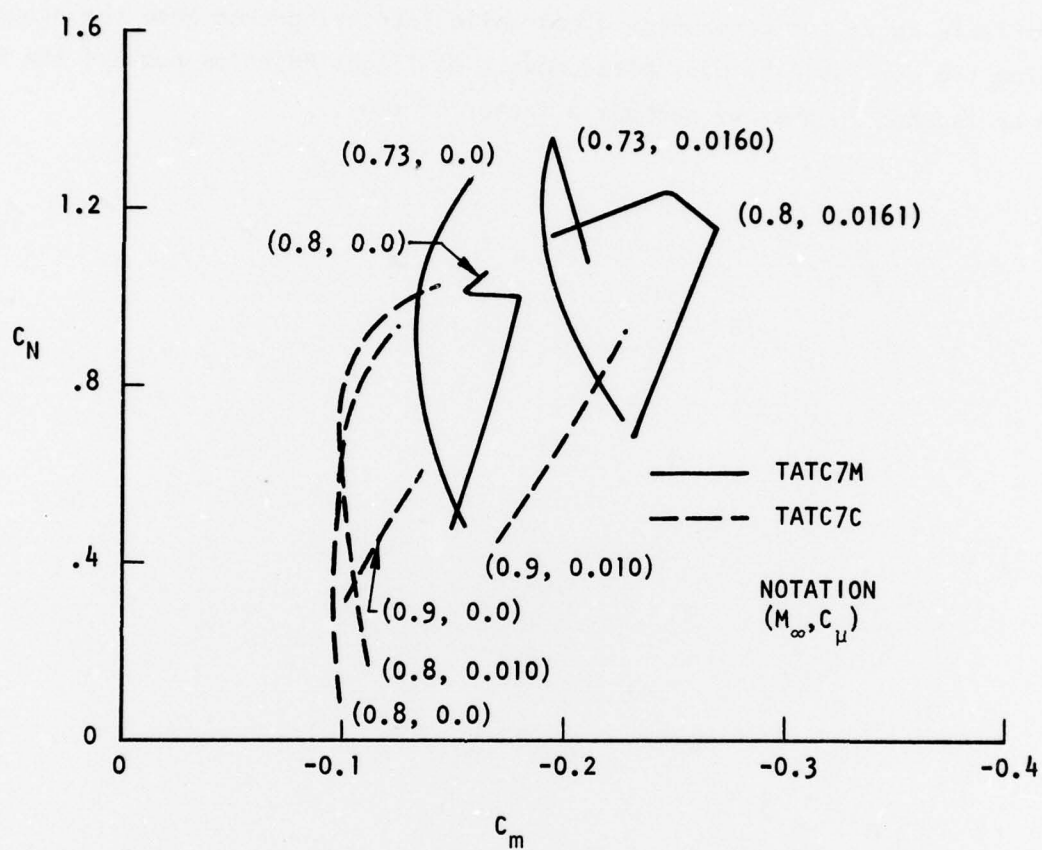


FIGURE 5-17 TATC7M, 7C AIRFOIL PITCHING MOMENT CHARACTERISTICS

show the predictions to be conservative. A $C_{\mu} = 0.005$ results in a significant maneuvering performance improvement, as evidenced by the $\Delta C_N = +0.13$ shown in Figure 5-12 for the TATC7M section relative to the Whitcomb baseline at equivalent drag. This data point is included in Figure 3-8 and is shown to approach the C_{μ} -available curve for compressor bleed while increasing even more the practicality of using the desirable by-pass bleed mode. At flight Reynolds numbers the $C_{\mu} = 0.005$ would be reduced further by perhaps a factor of two.

6.0 CONCLUSIONS

The use of advanced active diffusion control has resulted in cruise and maneuvering transonic airfoil design points which are similar enough to permit deployment from a common section while still achieving outstanding performance characteristics at both flight conditions. An airfoil thickness ratio of seven percent was selected because of the past attention given to thicker sections and the immediate need for innovative techniques in the thinner airfoil range. The antiseparation tailored contour (ATC) is a proven device for transonic active diffusion control.

Performance of the transonic ATC airfoil maneuvering and cruise geometries, designated TATC7M and TATC7C, respectively, has been validated in the Vought High Speed Wind tunnel. At a 0.8 Mach number and an equivalent drag ($C_d + C_{\mu}$), increments in maneuvering lift coefficient of +0.18 and +0.40 are indicated for the TATC7M section relative to Whitcomb-type airfoil predictions and conventional airfoil data, respectively. Data show drag divergence for the TATC7C deployment delayed at cruise lift coefficients by $\Delta M_{DD} = 0.08 - 0.09$ when compared with the Whitcomb-type reference. Equivalent drag polars define potential performance gains over a wide range of operating conditions. In addition to concept validations, the HSWT data provide comparisons with predictions that define required analytical refinements for design optimization (Section 7.0).

Because of the highly efficient ATC blowing, plenum pressure ratios in the 2-3 range are acceptable. Thus, in a perspective on engine bleed requirements, by-pass bleed becomes a viable alternative to the more conventional compressor bleed arrangements. Data for the ATC airfoil(s) show C_{μ} -required, even for maneuvering, to be a small fraction of the available by-pass bleed for existing engine technology and to be comparable to available compressor bleed when extrapolated to full-scale Reynolds numbers.

The above discussion of high Mach number design point performance for a variable geometry transonic section employing active diffusion control indicates the potential for unique performance and efficiency advantages in advanced airfoil design relative to purely passive approaches.

7.0 RECOMMENDATIONS

Although present analytical/empirical techniques have resulted in a successful design for a transonic blown airfoil, the development of an analytical tool to treat the problem of transonic jet mixing in an airfoil pressure field is needed to optimize blowing effects on section camber. Jet momentum coefficient measurements must also be refined to provide a data base for treating contouring/blowing sensitivity. A joint experimental/analytical effort of this type should also include consideration of leading edge geometry variations (droop, camber, etc.) in the context of further improving airfoil integration of ATC principles.

A second recommendation is to expand the test program to provide detailed scaling to higher Reynolds numbers. The present results indicate potential that must be verified at conditions approaching those of flight.

Transonic applications for highly loaded and/or low drag sections such as the ATC airfoil vary from aircraft cruise/maneuvering to missile lift/control, each with distinct planform requirements. Three-dimensional wing design studies are recommended to assess the performance potential of ATC sections for a range of typical aircraft/missile configurations.

8.0 REFERENCES

1. Whitcomb, R. T., "Review of NASA Supercritical Airfoils", Paper 74-10, Ninth Congress of the International Council of the Aeronautical Sciences, Haifa, Israel, August 25-30, 1974.
2. Yoshihara, H., Magnus, R., Carter, W., and Murray, R., "Lift Augmentation on Planar Airfoils in the Transonic Regime - A High Reynolds Number Wind Tunnel Study", Convair Aerospace Division Report No. CASD-NSC-73-001, Sept. 1973.
3. Yoshihara, H., Zonars, D., and Carter, W., "High Reynolds Number Transonic Performance of Advanced Planar Airfoils with Jet Flaps", AFFDL-TR-71-61, June 1971.
4. Haight, C. H., and Spangler, J. G., "Test Verification of a Transonic Airfoil Design Employing Active Diffusion Control", Final Report, NADC Contract No. N62269-74-C-0517, June 1975, also ATC Report No. B-94300/5CR-34, June 1975.
5. Haight, C. H., Reed, T. D., and Morland, B. T., "Design Studies of Transonic and STOL Airfoils with Active Diffusion Control", Final Report, NASC Contract No. N00019-73-C-0426, June 1974, also ATC Report No. B-94300/4CR-24, July 1974.
6. Krall, K. M., and Haight, C. H., "Wind Tunnel Tests of a Trapped Vortex High Lift Airfoil", Final Report, NASC Contract No. N00019-72-C-0379, Dec. 1972, also ATC Report No. B-94300/3TR-10, Jan. 1973.
7. Stivers, L. S., "Effects of Subsonic Mach Number on the Forces and Pressure Distribution on Four NASA 64A-Series Airfoil Sections at Angle of Attack as High as 28° ", NACA TN3162, 1954.
8. Young, A. D. "Note on Momentum Methods of Measuring Profile Drag at High Speeds", Ministry of Aircraft Production, February 1940.
9. Smith, D. K., "Wind Tunnel Investigations of the Pressure Distribution on a Two-Dimensional Airfoil with Pylon-Mounted Stores at Mach Numbers from 0.7 to 0.95, AEDC-TR-73-71, April 1973.
10. Evans, W., McKenzie, D., and Romanowski, R., "The Design, Test and Evaluation of Shockless Transonic Airfoils", NASC Contract No. N00019-72-C-0358, Grumman Aerospace Corporation, September 1973.
11. Whitcomb, R. T., and Clark, L. R., "An Airfoil Shape For Efficient Flight at Supercritical Mach Numbers", NASA TM X-1109, July 1965.
12. Whitcomb, R. T., "Basic Results of a Wind Tunnel Investigation of an Integral (Unslotted) Supercritical Airfoil Section", LWP-505, Nov. 1961.

Distribution List

Commander
Naval Weapons Center
China Lake, CA 93555

Commanding Officer
Naval Air Propulsion Center
Trenton, N.J. 08628

Commander
Naval Air Test Center
Patuxent River, MD 20670

Commander
David Taylor Naval Ship Research
& Development Center
Bethesda, MD 20034

Chief
Office of Naval Research
800 N. Quincy Street
Arlington, VA 22217

Institute of Defense Analysis
400 Army Navy Drive
Arlington, VA 22202
Attn: J. Attinello

Superintendent
Naval Postgraduate School
Monterey, CA 93940

Commanding Officer
Army Aviation Systems Test
Activity
Edwards AFB, CA 93523

Commanding General
Army Aviation Systems Command
St. Louis, MO 63102

Director
National Aeronautics & Space
Administration
Moffett Field, CA 94035
Attn: S. Anderson

Director
National Aeronautics & Space
Administration
Flight Research Center
Edwards AFB, CA 93523

Director
National Aeronautics & Space
Administration
Langley Research Center
Hampton, VA 23365

Director
National Aeronautics & Space
Administration
Lewis Research Center
2100 Brooke Park Road
Cleveland, OH 44135

Director
Air Force Flight Dynamics Laboratory
(ASD/ENFDH)
Wright-Patterson AFB
Dayton, Ohio 45433

Commander
Air Force Aeronautical Systems Division
Wright-Patterson AFB
Dayton, Ohio 45433

Commander
Air Force Flight Test Center
Edwards AFB, CA 93523

Commander
Naval Air Systems Command (AIR-954)
Department of the Navy
Washington, D.C. 20361
(10 copies):

(2) for retention
(5) for AIR-32D
(1) for AIR-5301
(1) for PMA-257
(1) for AIR-03PA

Administrator
Defense Documentation Center for
Scientific & Technical Information
(DDC)
Bldg. #5, Cameron Station
Alexandria, VA 22314
(12) copies

The Boeing Company
Seattle, WA 98101

LTV Aerospace Corporation
Dallas, Texas 75221

Rockwell International
Los Angeles, CA 90053

McDonnell-Douglas Corporation
3855 Lakewood Boulevard
Long Beach, CA 90808

Hughes Aircraft Company
Culver City, CA 90230

Northrop Corporation
Hawthorne, CA 90250

Lockheed-Georgia Company
Marietta, GA 30061

Royal Aeronautical Establishment
Bedford, England
Attn: A. Woodfield

B. P. Osborne, Jr.
OAD/ET 50552
Room 3D1089
Pentagon
Washington, D.C. 20301

Commander
Naval Air Development Center
Warminster, PA 18974
8 copies:
(3) for Code 813
(5) for Code 6053

General Dynamics
Convair Division
P. O. Box 80986
San Diego, CA 92138

General Electric Company
Aircraft Engine Group
1000 Western Avenue
Lynn, MA 01910

Rockwell International
Columbus, OH 43216

General Dynamics Corporation
Ft. Worth, TX 76108

Fairchild-Republic Corporation
Farmingdale, Long Island, NY 11735

Lockheed-California Company
P. O. Box 551
Burbank, CA 91503

Pratt & Whitney Aircraft Division
Division of United Aircraft Corporation
East Hartford, CT 06108

Grumman Aerospace Corporation
Bethpage, Long Island, NY 11714

McDonnell-Douglas Corporation
P. O. Box 516
St. Louis, MD 63166